國 立 交 通 大 學

光電工程研究所

碩 士 論 文

整合多模梯形波導之多模干涉矽波導線交錯元件的研究

Study of multimode interference-based waveguide crossings
integrated with multimode tapers for silicon wire waveguides

研 究 生：邱家祥

指導教授：陳瓊華　教授

中 華 民 國 九 十 九 年 六 月

整合多模梯形波導之多模干涉矽波導線交錯元件的研究
Study of multimode interference-based waveguide crossings
integrated with multimode tapers for silicon wire waveguides

研 究 生：邱家祥　　　　　　　　　　Student：Chia-Hsiang Chiu

指導教授：陳瓊華　　　　　　　　　　Advisor：Chyong-Hua Chen

國 立 交 通 大 學
光 電 工 程 研 究 所
碩 士 論 文

A Thesis

Submitted to Department of Photonics & and Institute of Electro-Optical

College of Electrical Engineering

National Chiao Tung University

in partial Fulfillment of the Requirements

for the Degree of

Master

in

Electro-Optical Engineering

June 2010

Hsinchu, Taiwan, Republic of China

中 華 民 國 九 十 九 年 六 月

整合多模梯形波導之多模干涉矽波導線交錯元件的研究

學生：邱家祥　　　　　　　　　　　　　指導教授：陳瓊華 博士

國立交通大學 光電工程研究所

摘　　　要

　　在本論文中，我們使用微型化之多模梯形波導設計出一新穎之多模干涉矽波導交錯結構並且使用時域有限差分法模擬其光學特性。此微型化的梯形波導有效地將入射光場擴束，因此除了降低輸入(輸出)波導與多模干涉波導之間的傳輸損耗，並且減少在波導交錯位置所產生的串音干擾 (Crosstalk)。此外，微型化梯型波導的使用促使縮短於多模干涉波導產生自我成像的所需之距離，進而減小交錯結構所需之多模干涉波導長度少於兩倍的拍長。利用三維時域有限差分法，我們探討不同梯形波導及形狀對於多模干涉交錯結構的特性影響並且獲得一個整合寬度平方變化梯型波導的多模干涉波導交錯結構，其尺寸為 5800 × 5800 平方奈米，在 1550 奈米的波長下的插入損耗 為 0.15 分貝及串音干擾為 -42 分貝，並且擁有於 1500 奈米到 1600 奈米波段下的寬頻穿透頻譜。
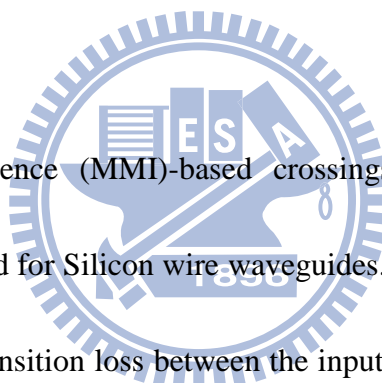
Study of multimode interference-based waveguide crossings integrated with multimode tapers for silicon wire waveguides

Student : Chia-Hsinag Chiu   Advisor : Dr. Chyong-Hua Chen

Institute of Electro-Optical Engineering

National Chiao Tung University

Abstract

Novel multimode-interference (MMI)-based crossings integrated with miniaturized tapers are numerically presented for Silicon wire waveguides. These miniature tapers function as field expanders to reduce transition loss between the input/output waveguide and the MMI waveguide and the crosstalk in the crossing region. As a consequence, the lengths of MMI waveguide reduce to less than twice of the beat length. Using finite difference time domain method, we demonstrate that the MMI-based waveguide crossing embedded in the quadratic tapers has the size of $5800 \times 5800 \ \text{nm}^2$, the insertion loss of 0.15 dB and the crosstalk of -42 dB at the wavelength of 1550 nm and broad transmission spectrum ranging from 1500 nm to 1600 nm.

誌謝

在碩士的生涯中，雖然只有短短的兩年，但在這期間也發生了很多事，讓我對許多事情有了新的體悟，也要感謝許多人的支持與幫忙，讓我能夠順利的完成碩士學位。首先我要感謝的就是我的指導老師陳瓊華教授，她是一位研究認真且為學生著想的好教授，老師除了在研究方面給我紮實的訓練與指導外，也跟我分享了很多人生的寶貴經驗，讓我在各個方面都獲益良多。

再來我要感謝李柏瑽教授、鄒志偉教授、何符漢博士能夠抽空來擔任我的碩士學位口試委員，並給予我在研究上的指導與肯定。還要感謝實驗室的各個成員，有洪瑋倫學長跟我分享在碩士班的經驗才讓我知道如何處理碩士班的事物，有侯紹璿學長跟我一起研究模擬軟體才能順利完成研究，還有感謝范日華可以跟我一起發洩壓力，感謝郁欣姐跟我一起闖過口試的難關，還有感謝翁一正幫忙處理實驗室的大小事，還有感謝唯一跟我同居的同學游文宏曾經陪我在碩一上一同修課。

還有要感謝紹平跟瑞泰一起接引我加入如來精舍，讓我能在妙禪師父的帶領下修行，還有感謝德正學長跟我分享禪行的心得解開我對禪修的疑惑，感謝妙禪師父的帶領，讓我在心情上能夠比較平靜，讓一切隨順圓滿。

再來要感謝我的家人對我的支持，讓我隨時有個溫暖的家可以依靠。最後我要感謝傑尼，在這一路以來，因為有你的支持與包容，我才能夠勇敢去面對所有遇到的難關，希望在人生未來的路上，我們能一起繼續走下去。

Content

List of Figure

List of table

Chapter 1 Introduction

1.1 Photonic Integrated Circuits and Silicon Photonics

In recent years, photonic integrated circuits (PICs) have attracted much attention due to the potential for replacing the integrated circuits (ICs) to achieve high speed and broad band data transmission. The basic optical components to implement a PIC include light sources, optical waveguides, modulators, and photodetectors, and they can be fabricated from a variety of materials like $LiNbO_3$, GaAs, InP, and silicon.

Silicon is conventionally used as a substrate for integrated circuits and recently Silicon photonics-an active research to realize photonic systems by using relatively cheap and abundant silicon as an optical medium-provides a platform for integrating electrical circuits and photonic circuits on a single chip. In addition, optical components made on a silicon on insulator[1] provides the advantages of low cost and small size due to being compatible with well-established CMOS fabrication techniques and high refractive-index contrast between silicon and silica.

Several high performance optical components for silicon photonics[2-3] have already presented in recent years. Low-loss silicon photonic wire waveguide had already studied with loss 0.5dB/cm [4-5]. The silicon modulator with 10 gigabits per second (10 Gbps) was presented by Ling Liao *et al.* [6]. A silicon-based avalanche photodetector (APD) with 40

Gbps data rate was presented by Intel [7]. To carry out monolithic optical integrated circuits, the difficulty in using silicon is silicon is an indirect bandgap material so as not to emit light. However, this issue was solved in 2005. A continuous wave silicon laser based on Raman scattering effect [8-9] was present by Intel. Because the light source issue was solved, silicon photonics is a promising candidate for the future computer industry.

1.2 Waveguide crossing

In PICs, waveguides are used to transit the optical signals among different optical components. When the waveguides are crossed, the optical signals are not affected by those in the other waveguides. As a result, the photonics circuits can be designed with grid-cross array and manufactured monolithically, as shown in Figure 1.2-1.
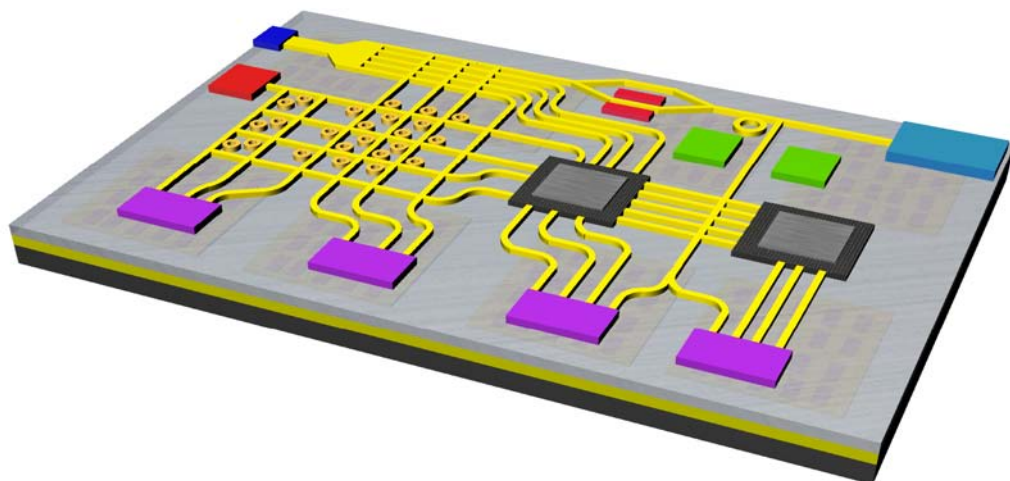
Figure 1.2-1 The diagram of a photonics circuit

As shown in Fig. 1.2-1, the waveguide crossings are indispensable for efficiently using the area of the substrate. However, in a direct waveguide crossing (i.e. two single-mode waveguides are 90° crossed), the field diverges and leaks at the crossing region because of high index-constrast between silicon and SiO_2.
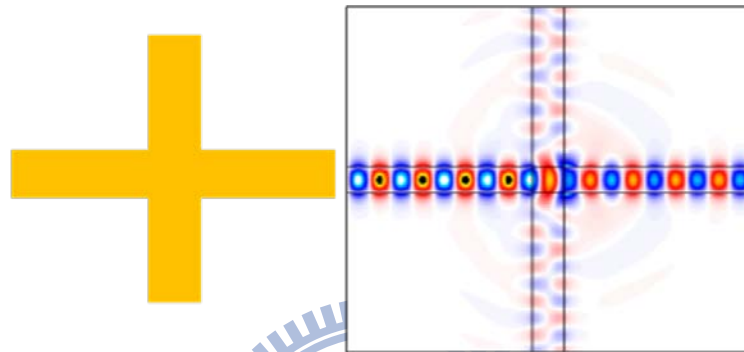
Figure 1.2-2 The direct waveguide crossing and the corresponding field distribution

Here we define the insertion loss and crosstalk of a waveguide crossing,

$$\text{Insertion loss} = -10\log\left(\frac{P_{out}}{P_{in}}\right), \qquad (\text{eq.}1.2\text{-}1)$$

$$\text{Crosstalk} = 10\log\left(\frac{P_{noise}}{P_{in}}\right), \qquad (\text{eq.}1.2\text{-}2)$$

where P_{in} is the power before entering the waveguide crossing, P_{out} is the power after propagating through the waveguide crossing, and P_{noise} is the power radiating into the orthogonal waveguide. The insertion loss of a direct crossing is 1.2 dB and its crosstalk is about -12 dB. In order to improve the performance of waveguide crossings, serveral structures are presented and we briefly introduce these designs as follows.

1.2.1 Mode expander waveguide crossing

The common structure of a waveguide crossing is a mode-expander waveguide crossing [10]. The mode expander expands the field wide to reduce the wide-angle components of the guided mode, thereby decreasing the diffraction of the field at the crossing region. The schematic structure and its field distribution are shown in Figure 1.2-3. The literature shows that the insertion loss is around 0.2 dB with its total length larger than 10 μm.
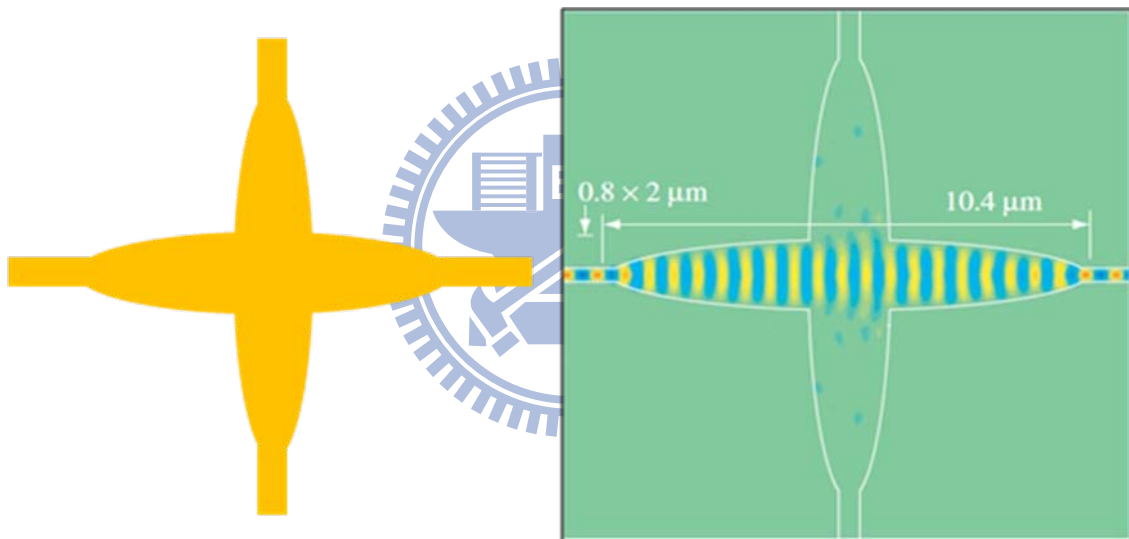
Figure 1.2-3 The mode expander waveguide crossing and the corresponding field distribution

1.2.2 Double etched mode expander waveguide crossing

The mode expander waveguide crossing with double etched was presented in 2007 [11] to reduce the size of this type waveguide crossing. Its structure and corresponding field distribution are displayed in Figure 1.2-4. The insertion loss is about 0.16 dB and its total size decreases to 6μm. However, double etched processes are required to realize this design and, as a result, the fabrication of this waveguide crossing becomes difficult and expensive,
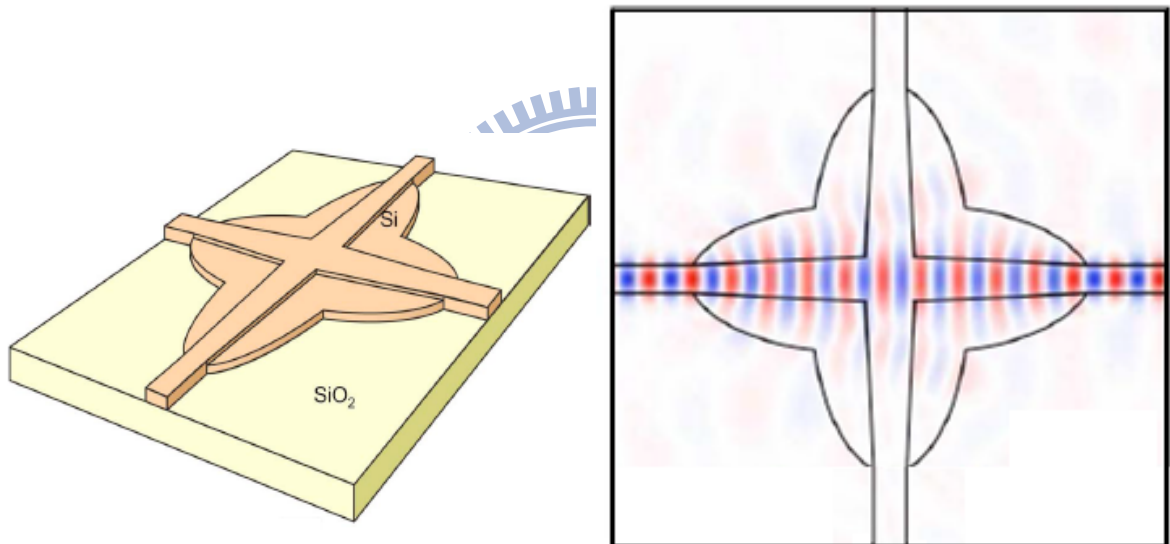
Figure 1.2-4 The double etched waveguide crossing and the corresponding field distribution

1.2.3 Highly efficient mode expander waveguide crossing

Highly efficient mode expander waveguide crossing [12] is a mode expander waveguide crossing without double etched processes. The total size is 6×6 μm^2 and the insertion loss is around 0.2 dB. Although this structure doesn't need to be fabricated by using double etched processes, the profile of this crossing is optimized by using genetic algorithm and becomes complex for the CMOS fabrication. In addition, the footprint of this design is still occupied by 6×6 μm^2, as shown in Figure 1.2-5.
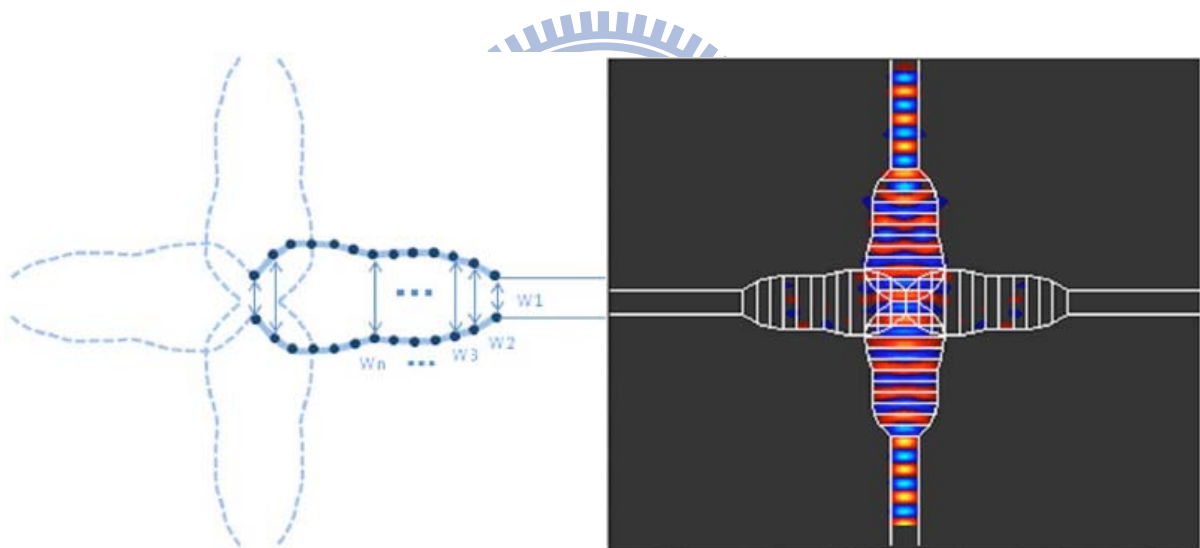
Figure 1.2-5 The highly efficient mode expander waveguide crossing and the corresponding field distribution

1.2.4 Metamaterial filled waveguide crossing

This waveguide crossing is filled metamaterial in the crossing region with impedance match [13] as displayed in Figure 1.2-6. The field passes though the crossing region without reflecting from the interface between input waveguide and crossing region because large refractive index of the metamaterial is used to confine the light at the metamaterial-filled crossing region. The insertion loss of this waveguide crossing is 0.04 dB and the total size is 600×600 nm^2. Although Ultra-low loss and ultra-small size can be achieved in this design, fabrication of this structure is difficult and expensive.
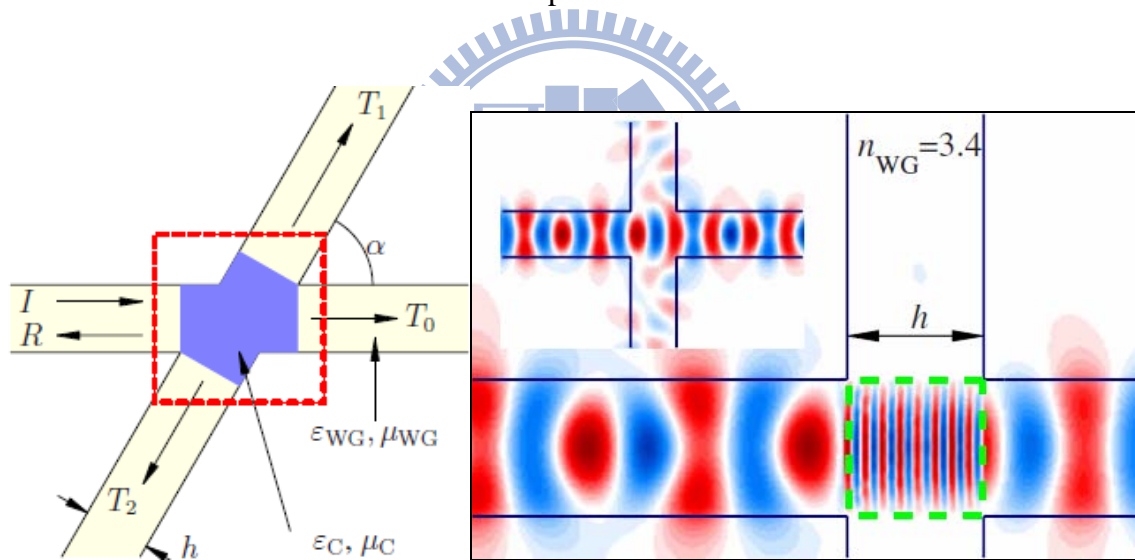
Figure 1.2-6 The metamaterial filled waveguide crossing and the corresponding field distribution

1.2.5 Multimode-interference-based waveguide crossing

Figure 1.2-7 shows the field propagates along a multimode-interference (MMI)-based waveguide crossing and we can observe a narrowing field at the crossing region [14-15]. Due to suppressing the field divergence at the crossing region, the insertion loss is reduced to around 0.2 dB. The total size of MMI-based crossing is 13×13 μm^2 and this size is too large to implement compact PICs.
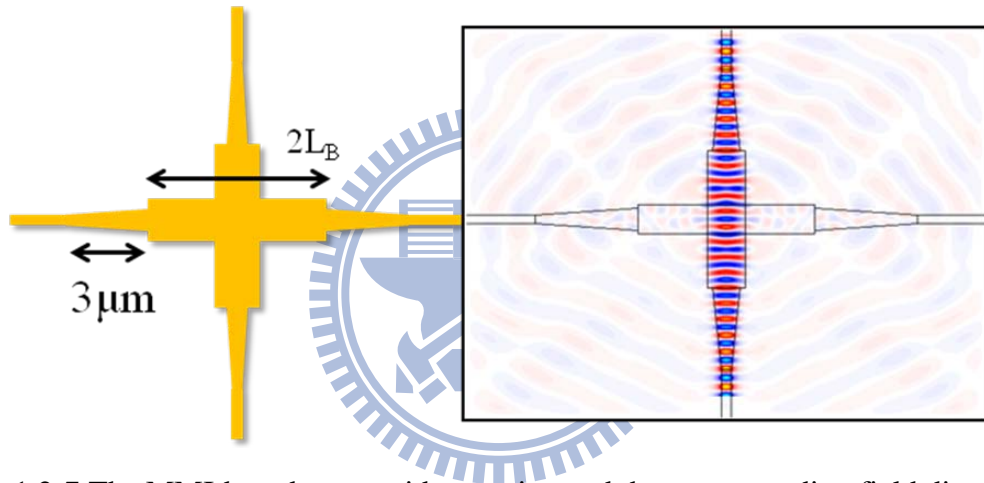
Figure 1.2-7 The MMI-based waveguide crossing and the corresponding field distribution

All the structures of waveguide crossings mentioned above have the problems of large footprints and complex fabrication processes. Here, we would like to present a novel MMI-based waveguide crossing with low insertion loss and small size. In addition, the requirement of fabrication techniques is compatible with current standard CMOS fabrication technique.

1.3 Organization

The organization of this thesis is described as follows. First, we introduce the mode expansion method for MMI waveguide and tapers in chapter 2. Next, the design approach to design a compact, low insertion loss and small crosstalk MMI based waveguide crossing is presented in chapter 3. At last, chapter 4 concludes this thesis.
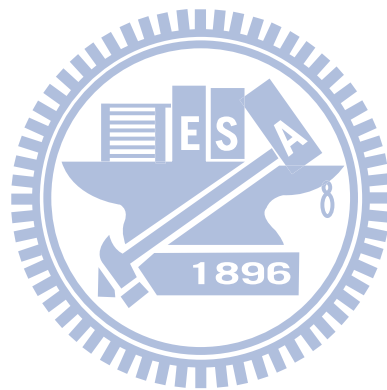
Chapter 2 Theories

In this chapter, we introduce the concept of the self-image principle which is the fundamental mechanism to design a MMI-based waveguide crossing. Next, the mode expansion method is presented for designing single-mode and multimode tapers.

2.1 Self-imaging principle

Self-imaging principle is the phenomenon that the field formed periodically in a multimode waveguide. In a multimode waveguide, there are several modes in this waveguide with their mode profiles and propagation constants. As some arbitrary field is impinged into the multimode waveguide, more than one mode are excited and each mode interfere to each other during propagating along the multimode waveguide, resulting in periodic multimode-interference distributions along the propagating direction. This kind of the multimode waveguide is called the MMI waveguide.

When an arbitrary field $E_{in}(x,y)$ is incident into a MMI waveguide, the field profile $E_{in}(x,y)$ can be decomposed into several modal field distributions $TE_i(x,y)$ which are the eigenmodes of the MMI waveguides and given by

$$E_{in}(x, y) = \sum_{i=0}^{N} C_i TE_i(x, y) \qquad (\text{eq.} \, 2 \text{-} 1)$$

where C_i is the modal coefficient of the mode field distribution $TE_i(x,y)$, i=0..N, and calculated by using overlap integral

$$C_i = \frac{\iint TE_{in}(x, y)TE_i(x, y)dxdy}{\iint TE_i(x, y)TE_i(x, y)dxdy} \qquad \text{(eq. 2 - 2)}$$

The electrical filed at the arbitrary position z in a MMI waveguide is

$$E(x, y, z) = \sum_{i=0}^{N} C_i TE_i \exp(-i\beta_i z) \qquad \text{(eq. 2 - 3)}$$

where z is propagating direction and β_i is the propagation constant of the mode field $TE_i(x,y)$.

When the field E(x,y,z) propagates along the waveguide direction z, the phase difference are induced among different modes because each mode has different propagating constant. The phase difference between modes changes from 0 to 2π, and the field profile E(x,y,z) in x-y plane at some distance z becomes the same as the incident field E_{in} as the phase difference becomes $2m\pi$, m is an integer. This phenomenon is named self-imaging principle[16] in the MMI waveguide.

Here, we give an example of the self-imaging principle in a three-mode supported MMI waveguide. Assume the incident field is the fundamental mode of an narrower waveguide, with centrosymmetric profile. From eq. 2-1, the input field $E_{in}(x,y)$ can be expressed by the two even modes of this three-mode supported MMI waveguide. By using overlap integral, the modal coefficient C_0 and C_2 for these lowest two even modes are obtained. Accordingly, the field E(x,y,z) in the MMI waveguide can be written

$$E(x, y, z) = C_0 TE_0(x, y) \exp(-i\beta_0 z) + C_2 TE_2(x, y) \exp(-i\beta_2 z) \qquad \text{(eq.2 - 4)}$$

where β_i is the propagation constant of the mode field $TE_i(x,y)$, i=0 and 2.

Figure 2.1-1 illustrates the field distribution E(x,y,z) in this MMI waveguide and we can

find the self-image reformed between some specific distance periodically. This specific

distance is defined as beat length L_B. In this example, the beat length can be calculated by

$$L_B = \frac{2\pi}{\beta_0 - \beta_2} \qquad \text{(eq. 2-5)}$$

The field distriution of field $E(x,y,z=mL_B)$ at mutliple beat length is simplified as

$$
\begin{aligned}
|E(x, y, z = L_B)| &= |C_0 E_0(x, y)\exp(-i\beta_0 L_B) + C_2 E_2(x, y)\exp(-i\beta_2 L_B)| \\
&= |\{C_0 E_0(x, y)\exp[-i(\beta_0 - \beta_2)L_B] + C_2 E_2(x, y)\}| \times |\exp(-i\beta_2 L_B)| \\
&= \left|\left\{C_0 E_0(x, y)\exp\left[-i(\beta_0 - \beta_2)\times\frac{2\pi}{\beta_0 - \beta_2}\right] + C_2 E_2(x, y)\right\}\right| \times |\exp(-i\beta_2 L_B)| \\
&= |\{C_0 E_0(x, y) + C_2 E_2(x, y)\}| \\
&= |E(x, y, z = 0)| \qquad \text{(eq. 2-6)}
\end{aligned}
$$

At multiple beat length, the phase difference between the two even modes becomes $2m\pi$,

and ,as a resulting, the field at $z = 0$ and the field at multiple beat length are the same, as

shown in Figure 2.1-1.
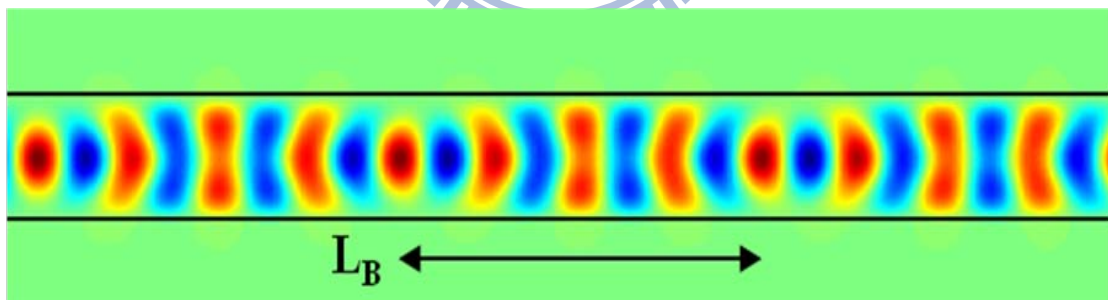
Figure 2.1-1 The periodic intensity distribution is formed along the propagating direction

2.2 Eigenmode expansion method for tapers

In the following section, we introduce the analysis of tapers by using eigenmode expansion method. Two types of the tapers are discussed- one is the single-mode taper and the other is the multimode taper. When the light propagates through the single-mode taper, the power of light is coupled from the input fundamental mode into the fundamental mode of another waveguide without converting to any higher-order modes of waveguides along the taper. When the light propagates through the multimode taper, the power is coupled into the fundamental mode and the other high modes of the multimode taper.

2.2.1 Single-mode tapers

A single-mode taper is a common component for mode conversion in PICs. As two different waveguides are connected, the mode profiles between them are different, resulting in the power loss as the power transfers from one waveguide to the other. To solve this issue, a single mode taper is inserted in between to convert the fundamental mode of one waveguide to that of the other to efficiently reduce the power loss due to the junction.

Here, , we use the eingenmode expansion method to analyze the power conversion along this gradually varied waveguide. Because the taper width is changed continuously along the propagation direction, we divide this taper into several discontinuous waveguides and approximate this taper to a cascaded waveguides with fixed waveguide width, as shown in

Figure 2.2-1. Each divided region is an individual waveguide with its corresponding eigenmodes. Assume this taper has its length of L_t and is divided into M parts, and then the length dz of each individual waveguide is L_t/M. The initial width is W_i and the finial width is W_f.
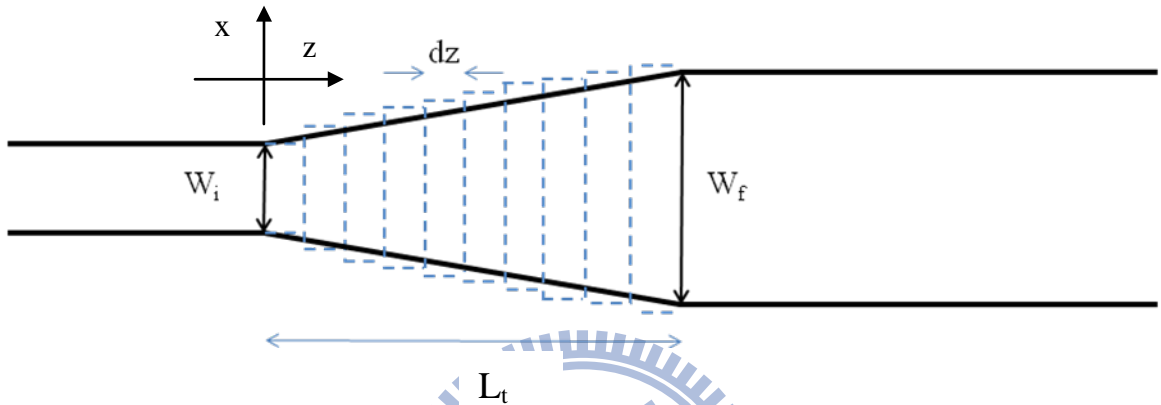
Figure 2.2-1 a taper is divided into several waveguide sections

First, when the input light incidents into the taper, the input field $E_{in}(x,y)$ is coupled into the modes of the first individual waveguide. According to eq. 2-1, the input field $E_{in}(x,y,z=0)$ can be expressed by the linear combination of eigenmodes in the first individual waveguide.

$$E_{in}(x, y, z = 0) = \sum_{i=0}^{N} C_i^{m=1} E_i^{m=1}(x, y) \qquad (eq. 2.2 - 1)$$

where m indicates the m-th individual waveguide and $C_i^{m=1}$ is the modal coefficient of the mode field distribution $E_i^{m=1}(x,y)$ in the first waveguide region , i=0..N, and calculated by using overlap integral

$$C_i^{m=1} = \frac{\iint E_{in}^{m=0}(x, y, z = 0)E_i^{m=1}(x, y)dxdy}{\iint E_i^{m=1}(x, y)E_i^{m=1}(x, y)dxdy} \qquad \text{(eq. 2.2 - 2)}$$

After the light propagates through the first waveguide, the field at the junction of the first and

second waveguides can be expressed by the eigenmodes of the second waveguide.

$$E_{in}^{m=1}(x, y, z = dz) = \sum_{i=0}^{N} C_i^{m=1} E_i^{m=1}(x, y)\exp\left(-i\beta_i^{m=1}dz\right) \qquad \text{(eq. 2.2 - 3)}$$

$$= \sum_{i=0}^{N} C_i^{m=2} E_i^{m=2}(x, y) \qquad \text{(eq. 2.2 - 4)}$$

By analogy with eq. 2.2-3 and eq. 2.2-4, we get the general relation between two

arbitrary neighbor waveguide regions m and m+1 as the following equation:

$$E_{in}^{m}(x, y, z = mdz) = \sum_{i=0}^{N} C_i^{m} E_i^{m}(x, y)\exp\left(-i\beta_i^{m}dz\right) \qquad \text{(eq. 2.2 - 5)}$$

$$= \sum_{i=0}^{N} C_i^{m+1} E_i^{m+1}(x, y) \qquad \text{(eq. 2.2 - 6)}$$

$$C_i^{m+1} = \frac{\iint E_{in}^{m}(x, y, z = mdz)E_i^{m+1}(x, y)dxdy}{\iint E_i^{m+1}(x, y)E_i^{m+1}(x, y)dxdy} \qquad \text{(eq. 2.2 - 7)}$$

Based on eq. 2.2-5 to eq. 2.2-6, the field at arbitrary position z can be obtained, and the power

at z can be calculated. Because the egienmodes are orthogonal, their relation can be described

as shown in eq. 2.2-8. The normalized total power at arbitrary m-th waveguide can be

simplified as eq. 2.2-10

$$\iint E_i^{m}(x, y)E_k^{m}(x, y) = \delta_{i,k} \qquad \text{(eq. 2.2 - 8)}$$

$$P^{m} = \iint \left(E_{in}^{m}\right)^{*}\left(E_{in}^{m}\right)dxdy \qquad \text{(eq. 2.2 - 9)}$$

$$= \sum_{i=0}^{N} \left|C_i^{m}\right|^2 = 1 \qquad \text{(eq. 2.2 - 10)}$$

When this taper functions as a single-mode taper, the fundamental mode in each

individual waveguide is excited as the input power is launched onto this taper. Therefore,

$|C_0^{m+1}|$ is approximately equal to one and $|C_i^{m+1}|$ for i=1…N have to be zero,. Assume only

fundamental mode is excited in the m-th waveguide, that is $C_0^m \neq 0$ and $C_1^m = C_2^m = C_3^m = ...$

$=C_N^m = 0$.

Eq.2.2-7 can be rewritten as:

$$\left| C_0^{m+1} \right| = \left| \frac{\iint C_0^m E_0^m (x, y) E_0^{m+1}(x, y) dx dy}{\iint E_0^{m+1}(x, y) E_0^{m+1}(x, y) dx dy} \right| = |\, C_0^m \,| \approx 1 \qquad (eq.\, 2.2\text{-}11)$$

$$\left| C_i^{m+1} \right| = \left| \frac{\iint C_0^m E_0^m (x, y) E_i^{m+1}(x, y) dx dy}{\iint E_i^{m+1}(x, y) E_i^{m+1}(x, y) dx dy} \right| = 0 \text{, where i} \neq 0 \quad (eq.\, 2.2\text{-}12)$$

Eq. 2.2-11 and eq. 2.2-12 are the basic conditions for a single-mode taper design. In

order to satisfy these conditions, the mode profiles of these two waveguides are almost similar.

Therefore, the widths of these two waveguide regions need to be almost the same. As shown

in Figure 2.2.1-1, the width difference between two connected waveguides dw is

$$dw = \frac{\left(W_f - W_i\right)}{L_t} dz \qquad (eq.\, 2.2\text{-}13)$$

Therefore, in order to have small dw, the length L_t of the single-mode taper has to be long and

the width change has to be slowly adiabatic.

2.2.2 Multimode tapers

Compared with the single-mode taper, the length L_t of a multimode taper can be short and the change of the width is fast. The power can be coupled into not only the fundamental mode but also the high-order modes. Similar to the previous analysis, we divide the multimode taper into several small waveguide regions. The field at arbitrary position is expressed by the eigenmodes of its local waveguide. However, due to fast variation on the taper width, reflection and transition powers at the interface of two connected waveguides have to be concerned, as shown in Figure 2.2-2.
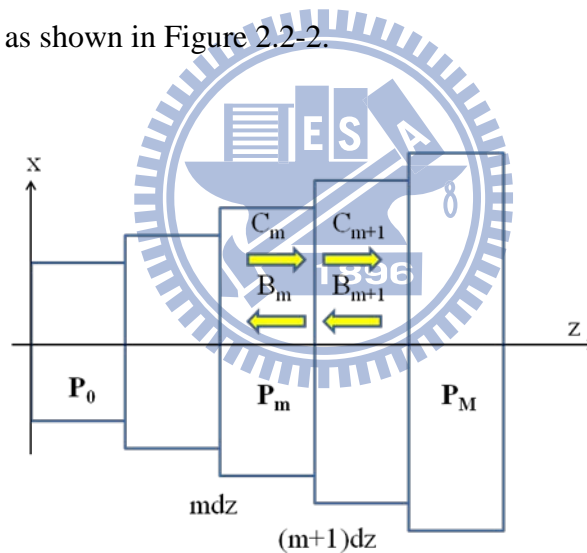
Figure 2.2-2 a multimode taper is divided into a series of individual waveguides with fixed width. Each section of the individual waveguide can be expressed by a transfer matrix P_m describing the amplitude variations of the forward and backward propagating modes at two adjacent sections

Here, we introduce the bidirectional mode expansion method for analysis of the multimode taper with TE case. In the m-th waveguide, both the forward and backward fields

17

are concerned and the field at arbitrary position z in the m-th waveguide can be written as

$$E_x^m(x, y, z = z) = \sum_{i=0}^{N} E_i^m(x, y)\left[C_i^m \exp\left(-i\beta_i^m(z - mdz)\right) + B_i^m \exp\left(i\beta_i^m(z - mdz)\right)\right] \quad \text{(eq. 2.2-14)}$$

$$H_x^m(x, y, z = z) =$$
$$\sum_{i=0}^{N} \frac{\beta_i^m}{w\mu_0} E_i^m(x, y)\left[C_i^m \exp\left(-i\beta_i^m(z - mdz)\right) + B_i^m \exp\left(i\beta_i^m(z - mdz)\right)\right] \quad \text{(eq. 2.2-15)}$$

where C_i^m is the modal coefficient for forward wave and B_i^m is the modal coefficient for

backward wave.

At the interface between the m-th and m+1-th waveguide, the tangential electric and

magnetic fields have to be continuous

$$E_y^m(x, y, z = (m+1)dz) = E_y^{m+1}(x, y, z = (m+1)dz) \quad \text{(eq. 2.2-16)}$$

$$H_x^m(x, y, z = (m+1)dz) = H_x^{m+1}(x, y, z = (m+1)dz) \quad \text{(eq. 2.2-17)}$$

By these two conditions, we obtain a transfer matrix P_m and the modal coefficients can be

calculated by the following relations

$$\begin{pmatrix} C^{m+1} \\ B^{m+1} \end{pmatrix} = P_m \begin{pmatrix} C^m \\ B^m \end{pmatrix} \text{ where } C^m = \begin{pmatrix} C_0^m \\ \vdots \\ C_N^m \end{pmatrix} , \ B^m = \begin{pmatrix} B_0^m \\ \vdots \\ B_N^m \end{pmatrix} \quad \text{(eq. 2.2-18)}$$

When a multimode taper is connected to a MMI waveguide, the power is coupled into

several modes of the MMI waveguide. The field propagates at arbitrary position z in the MMI

waveguide is then written as

$$E_x^m(x, y, z) = \sum_{i=0}^{N} \left[C_i^M \exp\left(-i\beta_i(z - L_t)\right) + B_i^M \exp\left(i\beta_i(z - L_t)\right)\right] E_i^M(x, y) \quad \text{(eq. 2.2-19)}$$

$$\begin{pmatrix} C^M \\ B^M \end{pmatrix} = P_M \cdots P_m \cdots P_0 \begin{pmatrix} C^0 \\ B^0 \end{pmatrix} \qquad \text{(eq. 2.2 - 20)}$$

As the modes propagate through the taper, the propagation constant induces the phase term and the corresponding modal coefficients C^M and B^M become complex numbers. We rewrite the C^M and B^M by the amplitude term and phase term as eq. 2.2-21 and eq. 2.2-22

$$C_i^M = |C_i^M| \exp(-i\theta_i^C) \qquad \text{(eq. 2.2 - 21)}$$

$$B_i^M = |B_i^M| \exp(-i\theta_i^B) \qquad \text{(eq. 2.2 - 22)}$$

By taking the eq. 2.2-21 and eq. 2.2-22 into eq. 2.2-19, the field at any position is rewritten as eq. 2.2-23.

$$E_x^m(x, y, z) =$$

$$\sum_{i=0}^{N} \left[\left| C_i^M \right| \exp\left(-i\left[\beta_i(z - L_t) + \theta_i^C\right]\right) + \left| B_i^M \right| \exp\left(i\left[\beta_i(z - L_t) + \theta_i^B\right]\right) \right] E_i^M(x, y) \qquad \text{(eq. 2.2 - 23)}$$

From eq. 2.2-23, we find each mode has an initial phase term, this phase term effects the distance of the first self-imaging. And the modal coefficient decides the profile of self-image. Therefore, we can make the self-imaging occurs in a MMI waveguide by multimode taper. And we can control the property of multimode-interference by changing the structure of multimode taper.

Chapter 3 Design approach

In this chapter, we show the design approach to achieve compact waveguide crossing by integrating multimode tapers to the MMI based waveguide crossings. The output field at the junction of the MMI waveguide and the multimode taper is coupled into both fundamental mode and next high order mode of the MMI waveguide, and thus the self-image is formed at the crossing region to suppress the divergence of the field. Here, we use three dimensional finite difference time domain (FDTD) method[17] to discuss the effects of taper lengths ad profiles on the performances of the MMI based waveguide crossing and to find the optimize design parameters for achieving compact, small loss and low crosstalk waveguide crossings.

3.1 Structure of the designed MMI based waveguide crossing

The structure of our designed MMI based waveguide crossing is displayed in Figure 3.1-1. The device is made on a silicon on insulator substrate where the Silicon (n=3.45) with thickness of 220 nm is deposited on a SiO_2 buffer layer (n=1.45). The input and output waveguides with width W_g of 500 nm are single-mode. The crossing region is composed of two 90° intersected MMI waveguides with lengths of L_m and widths W_m of 1200 nm to support three modes in MMI waveguides. Multimode tapers are used to connect the input/output and the MMI waveguides. The length of the multimode taper is L_t and its width is varied from 500 nm to 1200 nm. The length of MMI waveguide L_m is chosen to be twice of the length to form a self-image at the crossing center.
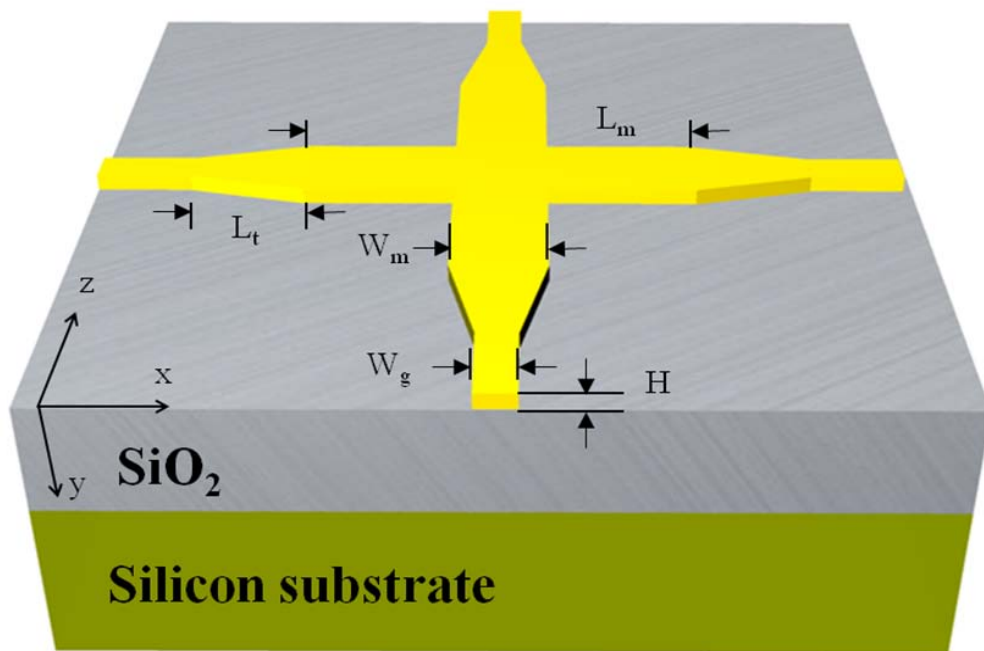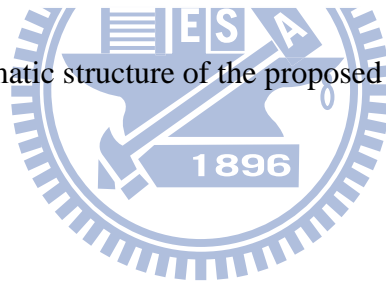
Figure 3.1-1 Schematic structure of the proposed waveguide crossing

3.2 Eigenmode properties of the input/output and MMI waveguides

Figure 3.2-1 shows the cross-section of the designed input waveguide and only the fundamental TE-like mode is supported in the input and output waveguides at the concerned wavelength of 1550 nm.
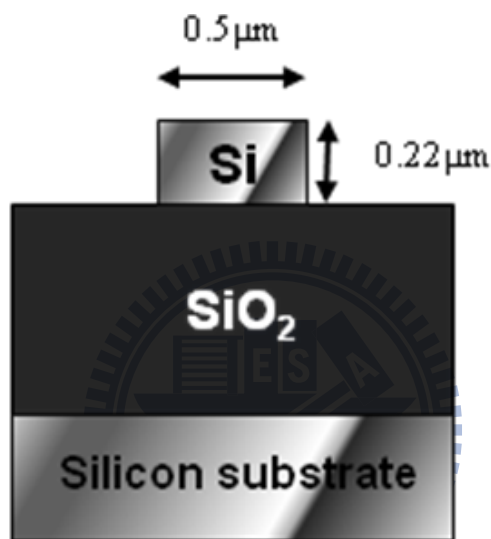

Figure 3.2-1 The cross-section of designed input/output waveguides

By using the Beam Propagation Method (BPM), the fundamental TE-like mode profile of the input waveguide is calculated and its mode distribution is shown in Figure 3-2. As shown in Fig 3.2-2, the power of the light is highly confined inside the silicon core. The effective index of this calculated mode is 2.034.
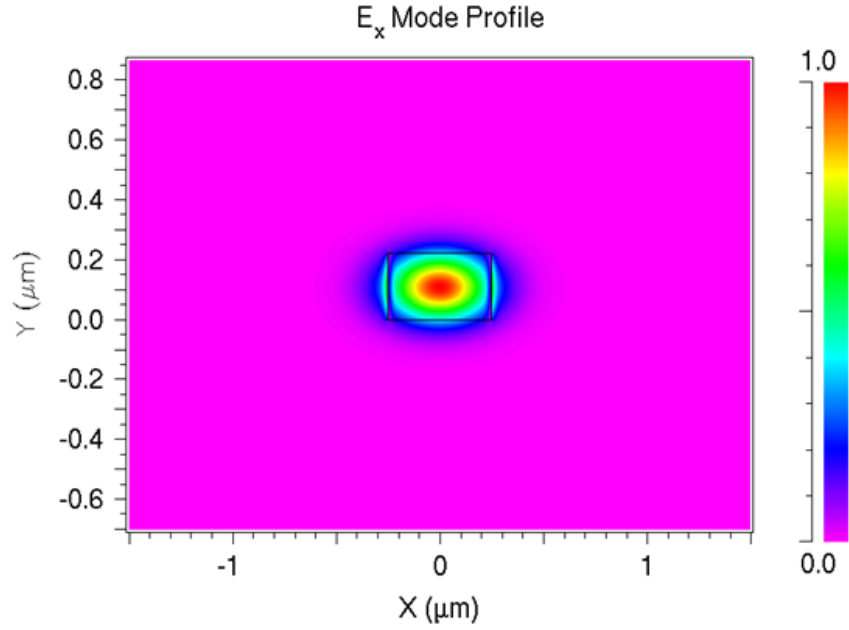
Figure 3.2-2 The fundamental mode profile of the input and output waveguides.

On the other hand, the width of the MMI waveguide (W_m) is designed to be 1200 nm and

its height (H) is the same as that of the input waveguide, i.e., H is 220nm.   In such design,

the MMI waveguide supports three TE-like modes (i.e., TE_{00}, TE_{01}, TE_{02} modes).   We

calculate the mode profiles of these TE-like modes by using BPM method. The calculated

mode profiles of these TE-like modes are shown in order in Figure 3.2-3 ~5.   According to

eq. 2-3, an arbitrary field propagating along the MMI waveguide can be linearly combined by

these three TE-like modes.

$$E(x, y, z) = C_0 TE_{00} e^{-i\beta_0 z} + C_1 TE_{01} e^{-i\beta_1 z} + C_2 TE_{02} e^{-i\beta_2 z} \qquad \text{(eq. 3.2-1)}$$

Let the field $E(x,y,z)$ be the fundamental mode of the input waveguide. Because the

fundamental mode is centrosymmetric in the x-direction as shown in Figure 3-2, C_1 is zero

calculated by overlap integral.   Therefore, the field inside the MMI waveguide is a linear

combination of TE_{00} and TE_{02} modes, and the self-image is observed as the phase difference

between these two modes becomes $2m\pi$, m is integer, i.e., the field of the self-image is

expressed as

$$E_y(x, y) = C_0 TE_{00} + C_2 TE_{02} \qquad\qquad (\text{eq.}\, 3.2\text{-}2)$$

Based on eq. 2-5, the beat length of the MMI waveguide is calculated as

$$L_B = \frac{2\pi}{\beta_0 - \beta_2} = 2271 \ (\text{nm}) \qquad\qquad (\text{eq.}\, 3.2\text{-}3)$$
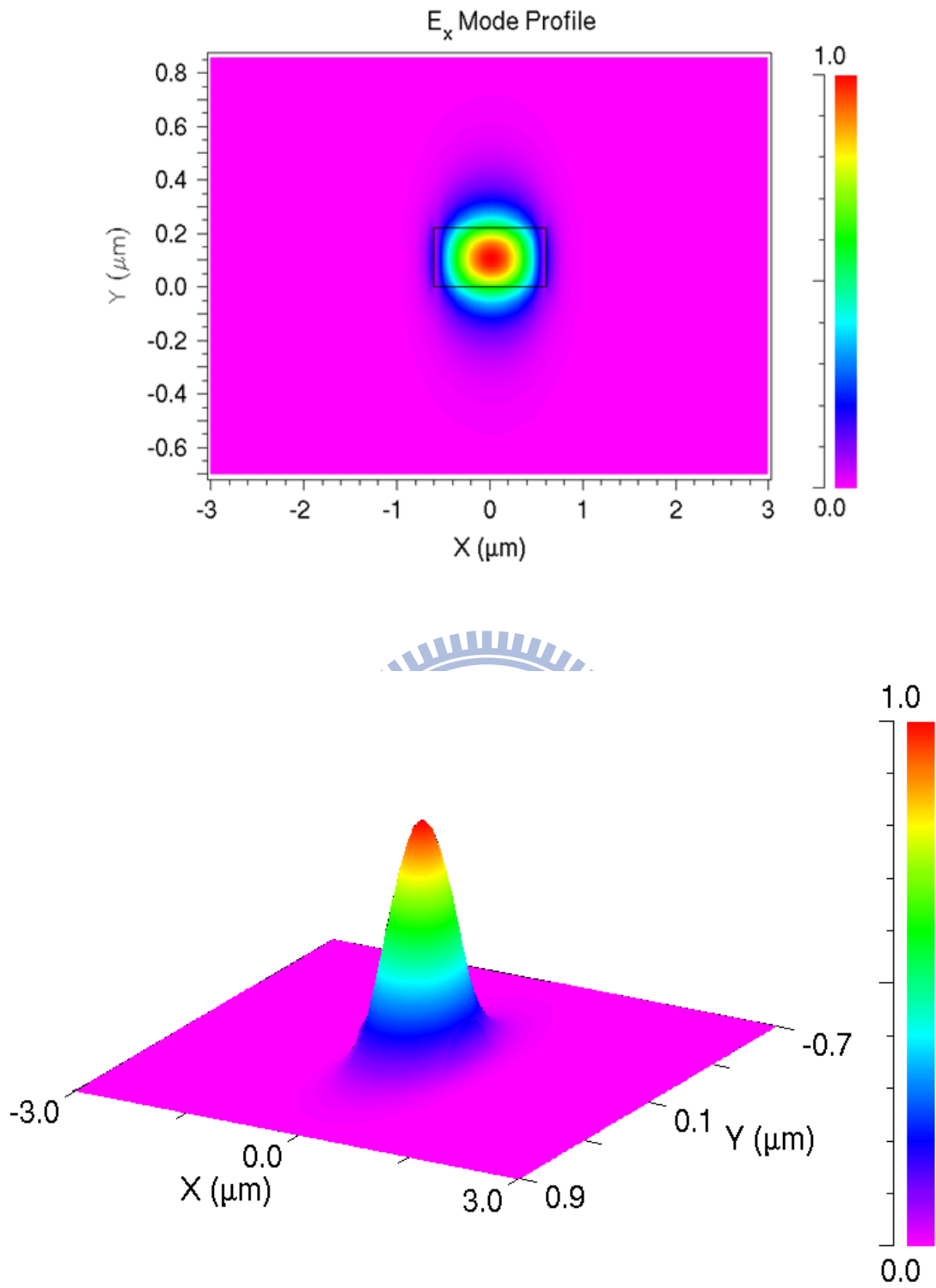
E_x Mode Profile

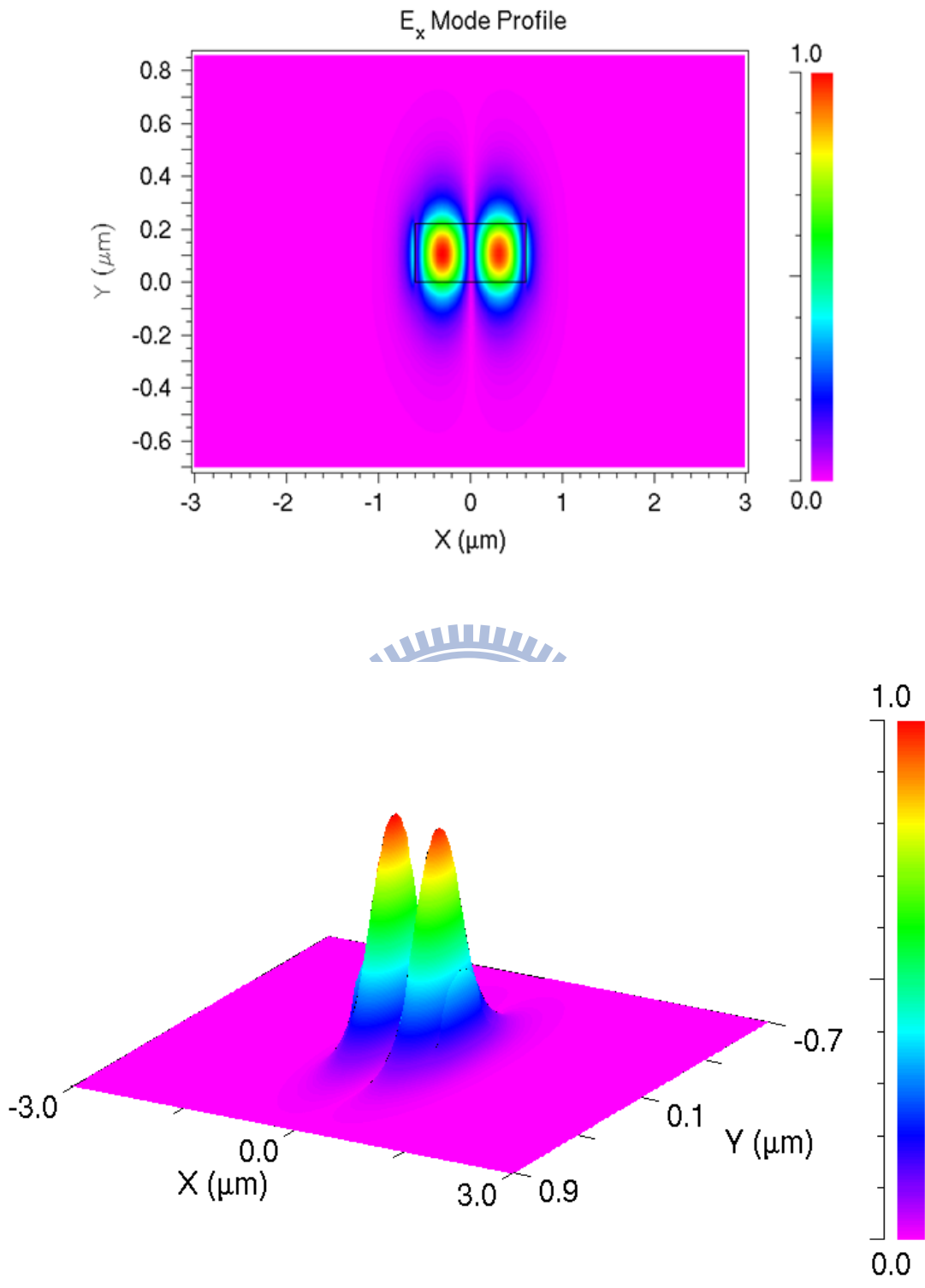Figure 3.2-3 The TE$_{00}$ mode distribution of the MMI waveguide.

Figure 3.2-4 The TE$_{01}$ mode distribution of the MMI waveguide.
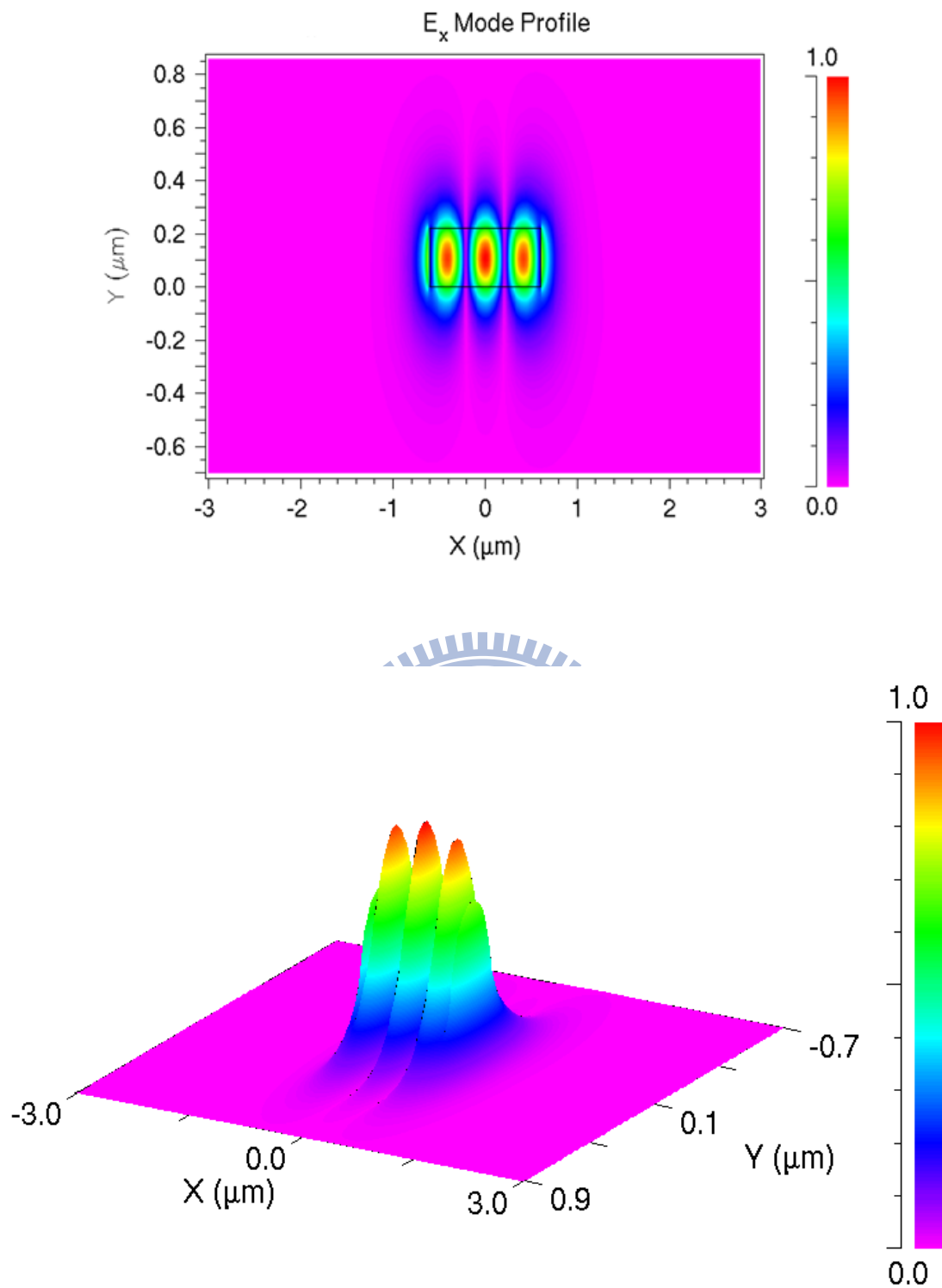
Figure 3.2-5 The TE$_{02}$ mode distribution of the MMI waveguide.

3.3 Diffraction loss with different self-image profiles

The major loss of a waveguide crossing is the loss at the crossing region because of vanish of lateral confinement there. We define the loss at the crossing region as diffraction loss and it can be calculated by

$$\text{Diffraction loss} = -10\log\left(\frac{P_{after}}{P_{before}}\right) \qquad (\text{eq. } 3.3\text{-}1)$$

where P_{before} is the power in the MMI waveguide before passing the crossing region and P_{after} is the power in the MMI waveguide after propagating through the crossing region.

The diffraction loss of a MMI based waveguide crossing is reduced because the a focusing self-image is formed at the crossing region. Here, we investigate the effect of the self-image profile on the diffraction loss by launching the field in the MMI waveguide constructed by different portion of TE_{00} and TE_{02} modes. From eq. 3.2-2, the input field profile can be decided by the modal coefficients of C_0 and C_2 , and we define the amplitude ratio η of C_2 to C_0 as

$$\eta = \frac{C_2}{C_0} \qquad (\text{eq. } 3.3\text{-}2)$$

The diffraction loss as a function of the amplitude ratio η is shown in Figure 3-3-1. The diffraction loss is about 0.6 dB at the ratio η of zero. As the ratio η increases, the diffraction loss decreases first and then increases as $\eta > 0.27$. At $\eta = 0.27$, the lowest diffraction loss is obtained, ~0.12 dB
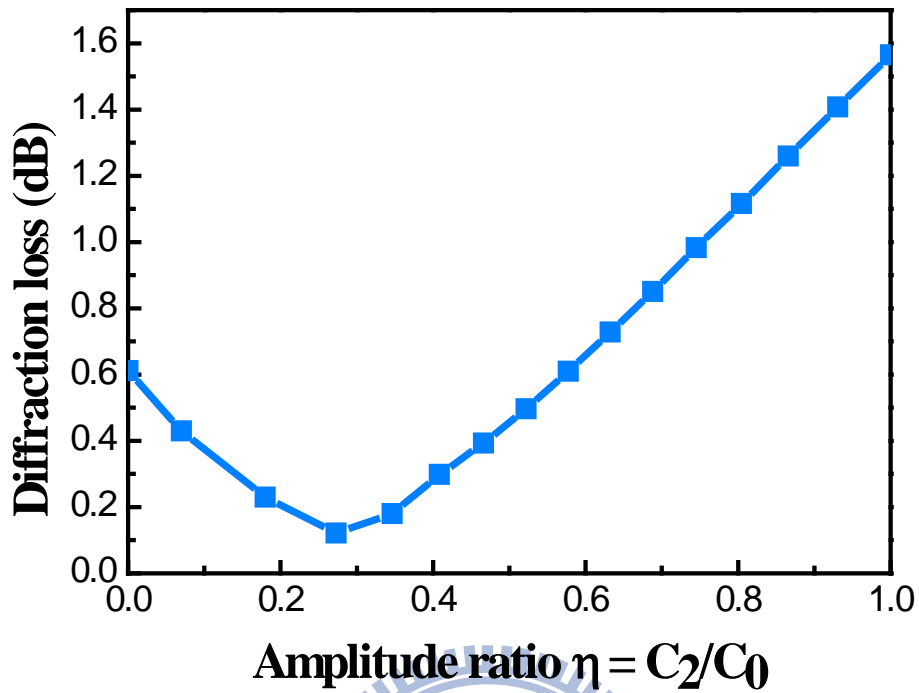
Figure 3.3-1 Diffraction loss as a function of amplitude ratio η

The corresponding self-image profile at different amplitude ratios are shown in Figure

3.3-2. As η increases from 0 to 0.27, the beam waist of the filed inside the guiding region

decrease and the field outside the guiding region also reduces, demonstrating a focusing beam

with narrow angular spectrum is obtained. At η=0.27, the field outside the guiding region is

approximately zero with the field profile well fit with a Gaussian function. On the contrary,

as η larger than 0.27, the beam waist inside the guiding region keep reducing but the field

outside the guiding region increases, showing the field has more amount of the high-angular

components and this results in more diffraction loss.

(a) η = 0.07

(b) η = 0.18
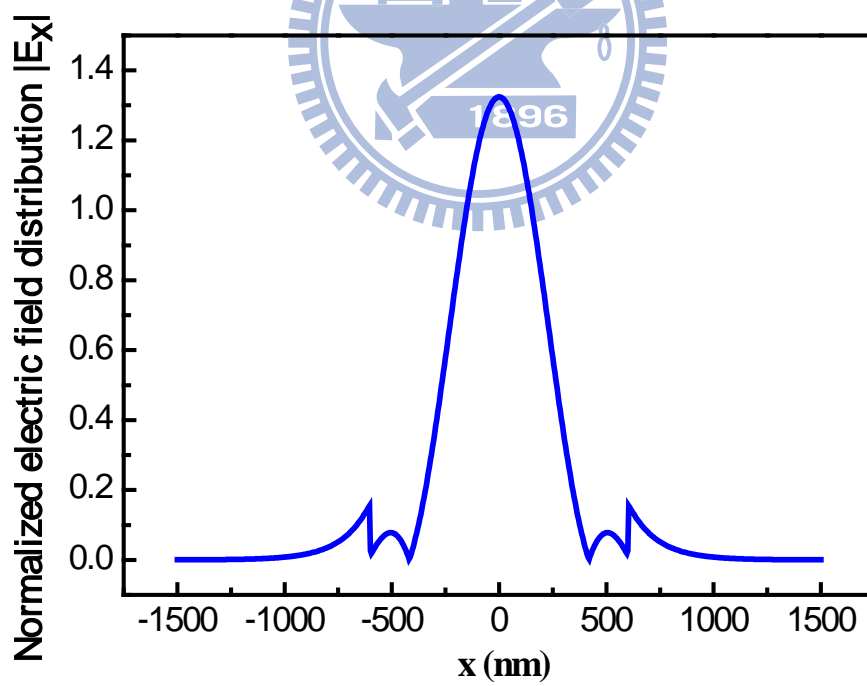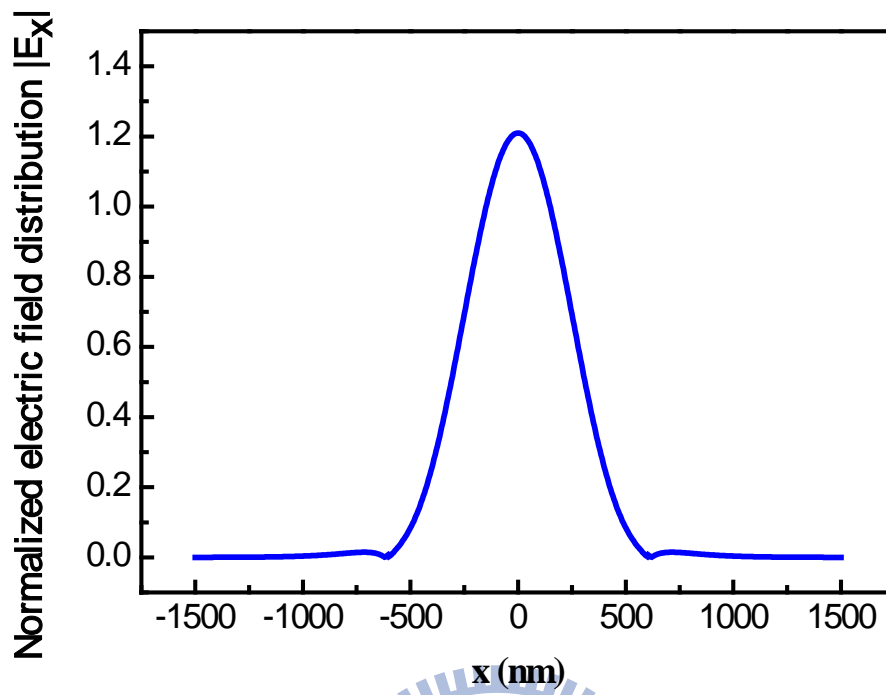
(c) η = 0.27

(d) η = 0.51
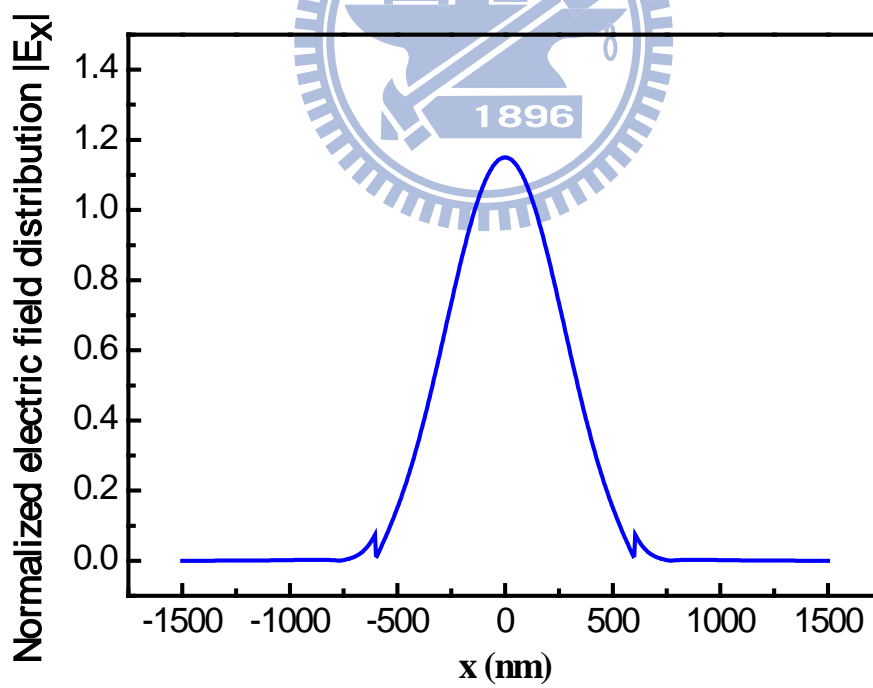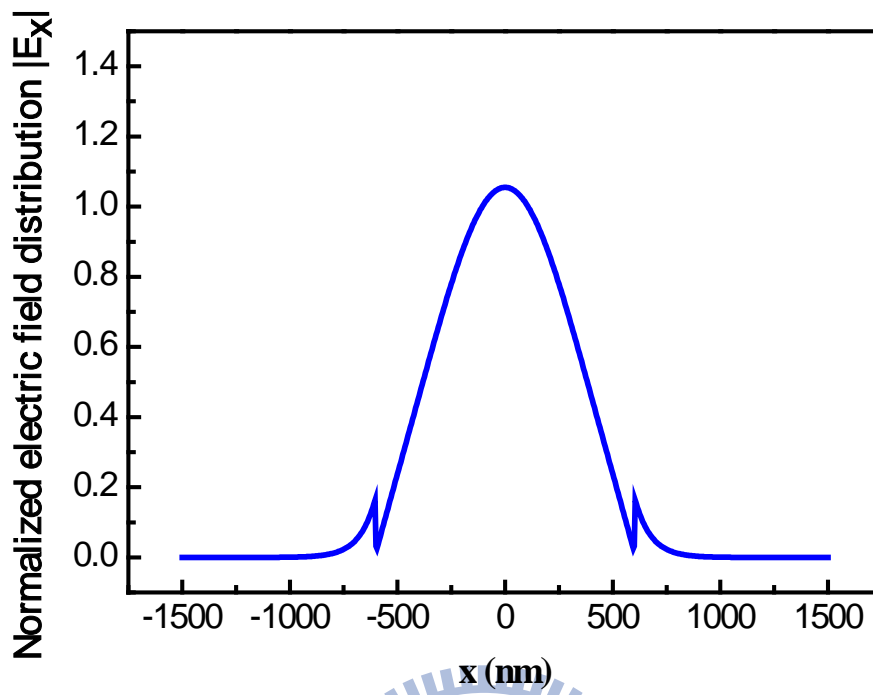
Fig. 3.3-2 Variations of field distributions normalized by the power of the self-image at amplitude ratio η of (a) 0.07, (b) 0.18, (c) 0.27 and (d) 0.51

3.4 Multimode taper design

Here, we study the effect of the taper length on the self-image profile in the MMI waveguide.   As shown in Figure 3.4-1, the taper width varies linearly from W_g to W_m with its length of L_t and taper height is fixed to be 220 nm. We change L_t from 0 to 2000 nm. Figure 3.4-2 shows the simulated electric field E_x propagating along the linear taper and the MMI section with different taper lengths. The lengths of these taper are (a) 0 nm, (b) 500 nm, (c) 1000 nm, and (d) 2000 nm, respectively. In the absence of the taper (i.e., L_t is 0 nm.), the input field is coupled into the two lowest even modes of the MMI waveguide (TE_{00}、TE_{02} modes) at the interface between the input and the MMI waveguide and the first self-image is formed after propagating 2271 nm (i.e. a beat length) in the MMI waveguide as shown in Figure 3.4-2 (a).
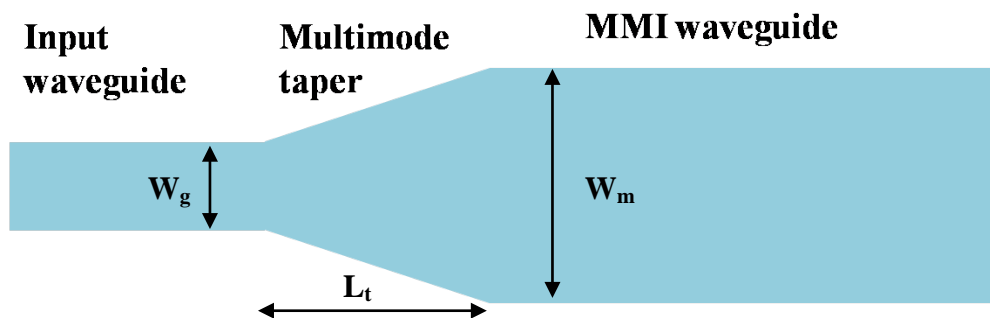
Figure 3.4-1 The diagram of a multimode taper

In the case of the taper length of 500 nm as shown in 3.4-2 (b), the beam width of the self-image becomes wider and the distance where the first self-image is formed becomes shorter than a beat length. Base on eq. 3.2-3, the beat length is constant for a given MMI waveguide. Here, we define the distance where the self-image is formed as the effective beat length L_{eff}. As the taper length increases, we see that the self-image profile and the effective beat length are different, and next we study the effect of the length of this linear taper on the amplitude ratio corresponding to the realized self-image profile, transition loss and the effective beat length.
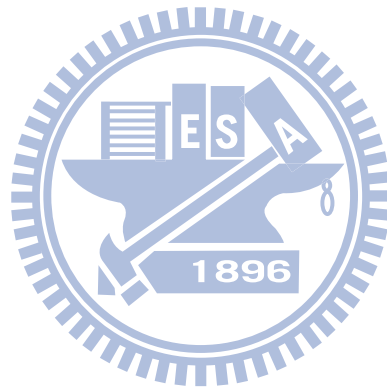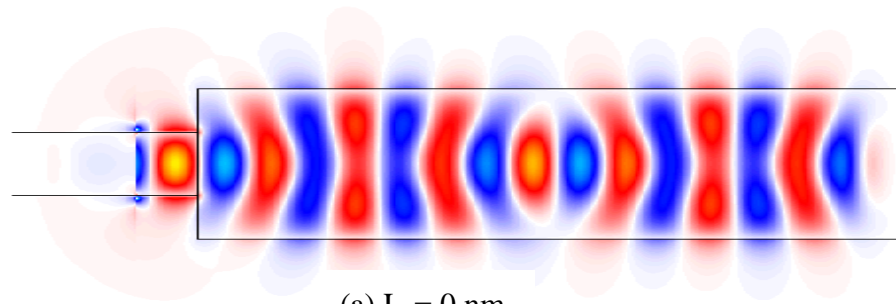
(a) $L_t = 0$ nm
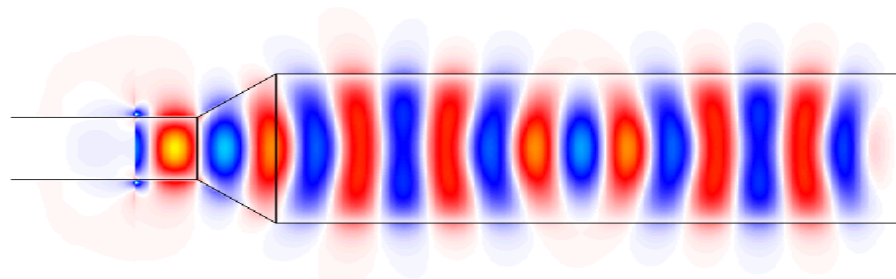
(b) $L_t = 500$ nm

(c) $L_t = 1000$ nm
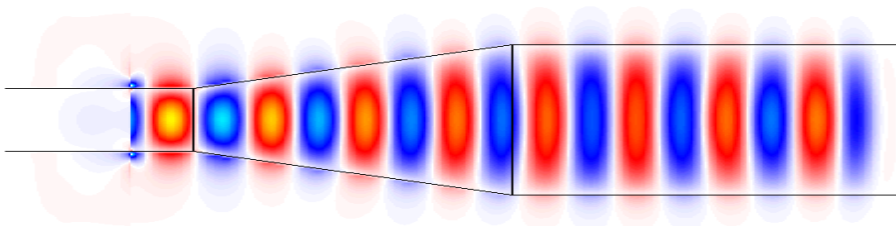
(d) Lt = 2000 nm

Figure 3.4-2 Evolution of the input guided mode propagation through the linear taper with its length of (a) 0, (b) 500, (c) 1000 and (d) 2000 nm and the MMI waveguide

3.4.1 Effect of taper length on the amplitude ratio η

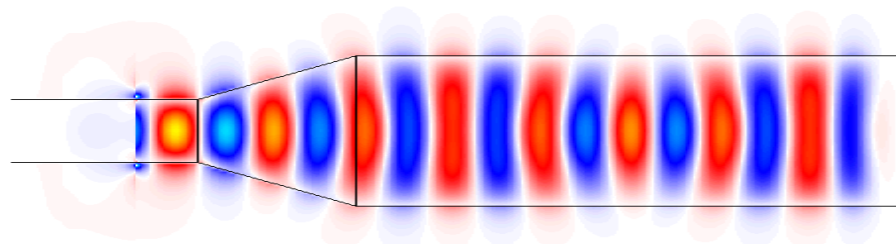As shown in Figure 3.4-2, the field distribution along the MMI waveguide is different as the taper length changes and we use overlap integral to acquire the modal coefficients of TE_{00} and TE_{02} modes for all cases of the different taper lengths.   The variation of the taper length on amplitude ratio is shown in Figure 3.4-3.
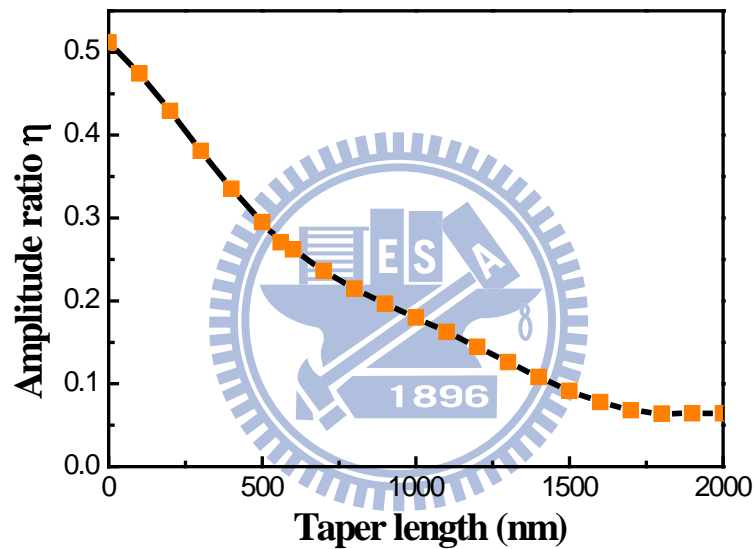
Figure 3.4-3 Variation of taper length on the amplitude ratio

As L_t=0 nm, 20.11% of the input field is coupled into the TE_{02} mode and the corresponding amplitude ratio is 0.51. As the taper length L_t increases, the power coupled into the TE_{02} mode decreases and thus the amplitude ratio η reduces monotonically.   In section 3.3, we obtained the lowest diffraction loss as η=0.27.   To achieve this condition, the length of this linear taper has to be 560 nm.

3.4.2 Effect of taper length on transition loss

Conventionally the taper is inserted in between two mismatched waveguides in order to reduce the transition loss. Here, we study the effect of taper length on the transition loss and the results are shown in Figure 3.4-4. As the taper length is zero, some input power is radiated and reflected at the interface of the input and MMI waveguides due to mode mismatch. By using overlap integral, the transition loss is calculated to be 0.226 dB, corresponding to the total coupling efficiency of 94.93%. As shown in Figure 3.4-4, the transition loss decreases with the increase of the taper length. In addition, the reduction of the transition loss is steep as the taper length increases from 0 to 1000 nm. The transition loss is smaller than 0.003 dB (i.e., the coupling efficiency is more than 99.93%) as the taper length is larger than 1000 nm. As the taper length is 560 nm, the transition loss is roughly equal to 0.08dB.
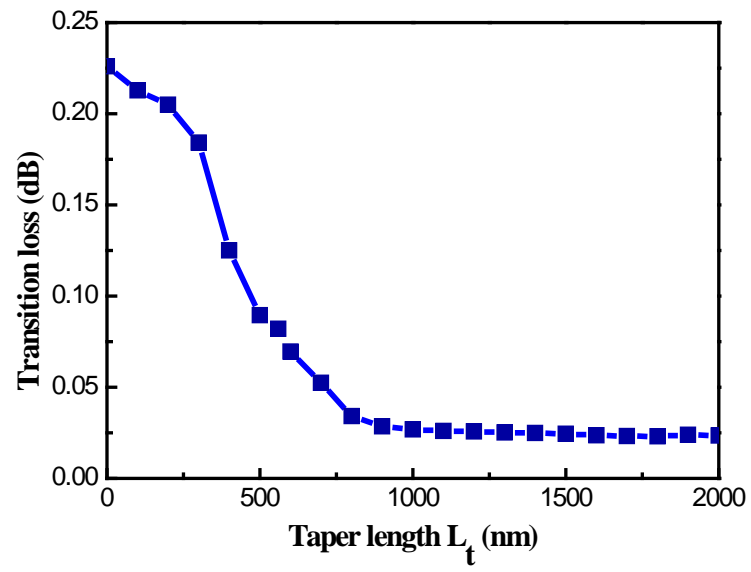
Figure 3.4-4 Transition loss as a function of the taper length

3.4.3 Effect of taper length on the effective beat length

We notice that L_{eff} are varied with the taper length in Figure 3.4-2. The variations of the effective beat length L_{eff} with the taper length L_t is displayed in Figure 3.4-5. Without inserting a taper (i.e., L_t=0 nm), the effective beat length is equal to the beat length. As the taper length L_t increases, the effective beat length L_{eff} decreases and is smaller than the beat length.
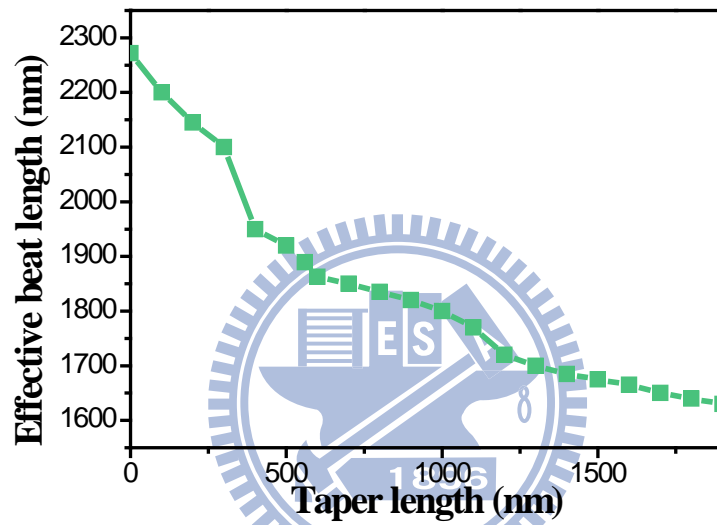
Figure 3.4-5 Effective beat length L_{eff} as a function of the taper length L_t.

When the field propagates through this multimode taper, a phase difference between TE_{00} and TE_{02} modes is induced at the junction of the multimode taper and the MMI waveguide because the modes interfere along this multimode taper. The self-image with phase difference of 2π is observed as the field propagates an effective beat length along the MMI waveguide. The effective beat length, therefore, can be calculated by

$$L_{eff} = \frac{2\pi - \text{initial phase difference}}{\beta_0 - \beta_2} \qquad (eq.\,3.4\text{-}1)$$

where initial phase difference is the phase difference of the TE_{00} and TE_{02} modes at the output

of the multimode taper.

As the taper length increases, the length for mode interference increases. As a result, the initial phase difference increases and the effective beat length decreases with the increase of the taper length.   As the taper length is 560 nm, the corresponding effective beat length is 1889.3 nm and the length of MMI waveguide is chosen to be twice of the effective beat length to implement a MMI waveguide crossing.

3.5 Performances of MMI based crossings with linear tapers

Figure 3.5-1 shows the FDTD simulation results of these taper-integrated MMI based waveguide crossings with the taper length L_t of 0 nm, 560 nm, 1000 nm and 2000 nm, respectively.   Here, the length of the MMI section in each design is chosen to be twice of the effective beat length obtained in the aforementioned section.   In the case of $L_t = 0$ nm, field is diffracted dramatically at the crossing region and significant scattering field radiates into the orthogonal MMI waveguide.   In the case of $L_t = 560$ nm, we see a narrowing field at the center of the crossing and the wave fronts at the front and back of the crossing are almost the same with reversal sign of phases. In the cases of the larger L_t, as shown in Figure 3.5-1 (c) and (d), the field scatters through the crossing region without significant crosstalk because the dominant component of the field is the TE_{00} mode with a narrow angular spectrum. However, we can see wave front expands more widely at the back of the crossing region, and this results in more insertion loss.

Table 1 lists the parameters and performance of these four taper-integrated MMI crossing structures with taper lengths of 0, 560, 1000 and 2000 nm, respectively. As η decreases, dimension of the crossing increases but the crosstalk decreases. The lowest insertion loss of these taper-integrated MMI based crossings is obtained as the taper length is 560 nm.

In the case of $L_t = 0$ nm, the diffraction loss is roughly equal to 0.58 dB and the insertion loss (~0.78 dB) is roughly equal to the sum of the transition loss (0.226 dB) and diffraction loss, meaning 16.44% of the input power is lost after the filed propagates through the MMI based waveguide crossing without inserting a taper. In the case of L_t=560 nm (for $\eta = 0.27$), the diffraction loss is about 0.12 dB and its insertion loss is 0.24 dB.

In the cases of $L_t = 1000$ nm and 2000 nm, the field diverges at the crossing region such that the guided modes of the MMI waveguide and the diverged field at the back of the crossing are mismatch, resulting in substantial insertion loss. Compared with the MMI based crossing without inserting tapers (i.e. the case of $L_t = 0$), the taper-integrated MMI based crossings perform smaller insertion loss and less crosstalk.
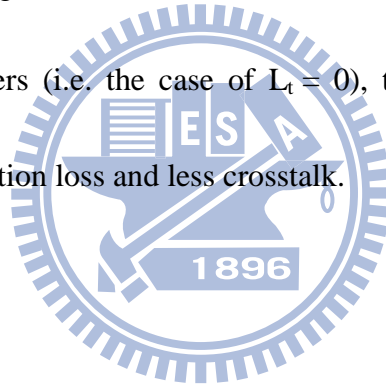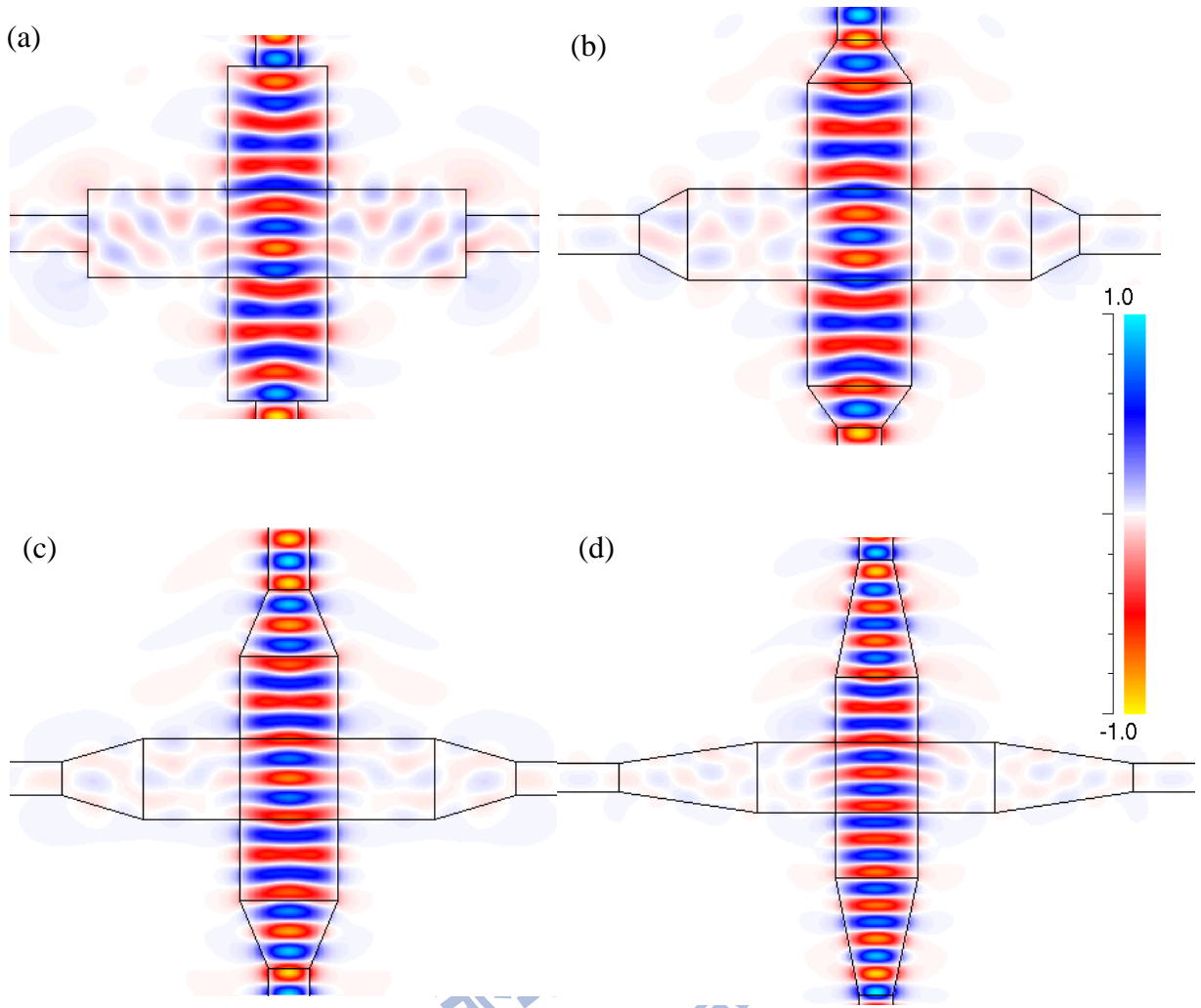
Figure 3.5-1 FDTD simulations of the input guided mode propagation through
MMI based waveguide crossings sandwiched by four identical linear tapers
with (a) L_t=0 and L_m=4543.4 nm, (b) L_t=560 nm and L_m=3778.5 nm, (c)
L_t=1000 nm and L_m=3600 nm and (d) L_t=2000 nm and L_m=3450.4 nm.
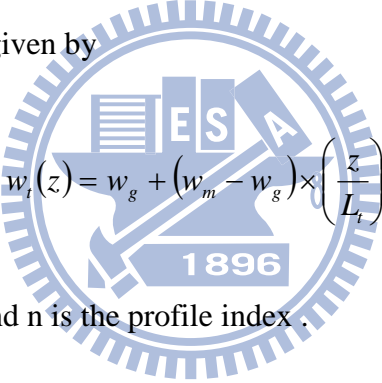
Table 1 Properties of MMI based waveguide crossings integrated with linear tapers at the
wavelength of 1550 nm

L_t (nm)	η	L_{eff} (nm)	L_m+2L_t (nm)	Insertion loss (dB)	Crosstalk (dB)
0	0.52	2271.7	4543.4	0.78	-23.19
560	0.27	1889.3	4898.5	0.24	-45.39
1000	0.18	1800.0	5600.0	0.25	-48.12
2000	0.07	1725.2	7450.4	0.43	-50.63

3.6 Effect of the Taper Profiles

In the previous section, we realized the smallest insertion loss as the amplitude ratio $\eta = 0.27$. In order to achieve this value, the corresponding linear taper length L_t is 560 nm, and, as a consequence, the transition loss of this taper is 0.08dB and the effective beat length is 1889.3 nm.

Here, we investigate the effect of the taper profiles on the transition loss and the effective beat length. The studied taper profiles expand in width with an initial value of 500 nm to the final value of 1200 nm and are given by

$$w_t(z) = w_g + \left(w_m - w_g\right) \times \left(\frac{z}{L_t}\right)^n \qquad\qquad (eq.\,3.6\text{-}1)$$

where $w_t(z)$ is the taper width and n is the profile index .

Here, we chose the taper profiles with n = 0.25, 0.5, 1 and 2 and the corresponding L_t are 750, 530, 560 and 1000 nm in order to realize $\eta=0.27$.

The field distributions along these four taper and MMI sections are shown in Figure 3.6-1. In the case of n=0.25 and n=0.5, the width varies steeply, and, as a result, the effective beat length for each design decreases to be 1400 nm and 1735 nm, respectively. However, the transition loss is larger than the case of the linear taper. In the case of n=2, the transition loss is 0.02 dB with longer effective beat length (1900 nm).
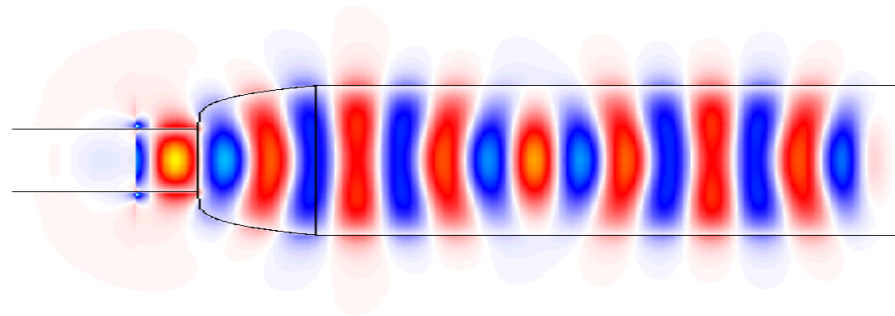
(a) $L_t = 750$ nm, n=0.25
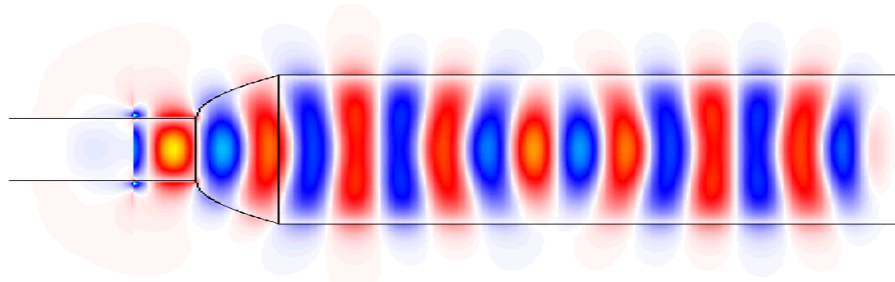
(b) $L_t = 530$ nm, n=0.5
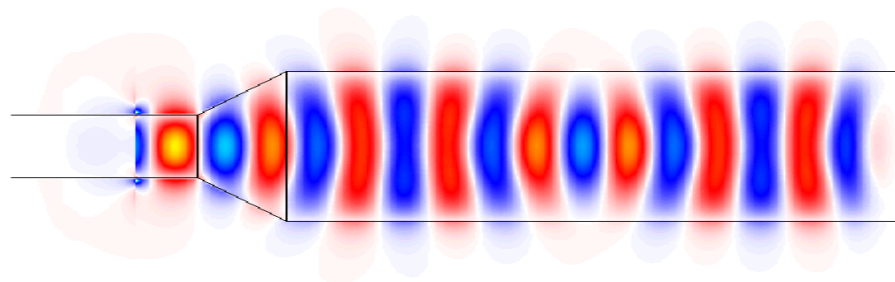
(c) $L_t = 560$ nm, n=1

(d) $L_t = 1000$ nm, n=2

Figure 3.6-1 Evolution of the input guided mode propagation through different taper profiles with n= (a) 0.25, (b) 0.5, (c) 1 and (d) 2 and the MMI waveguide

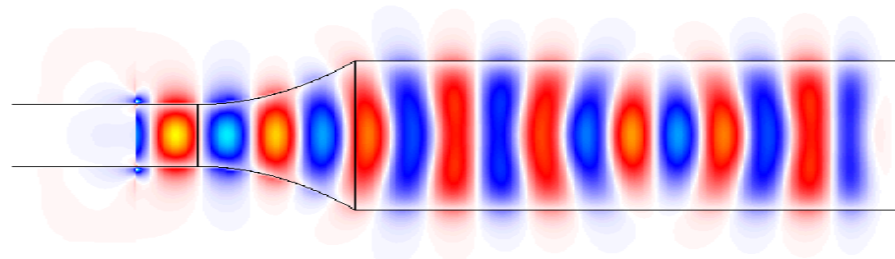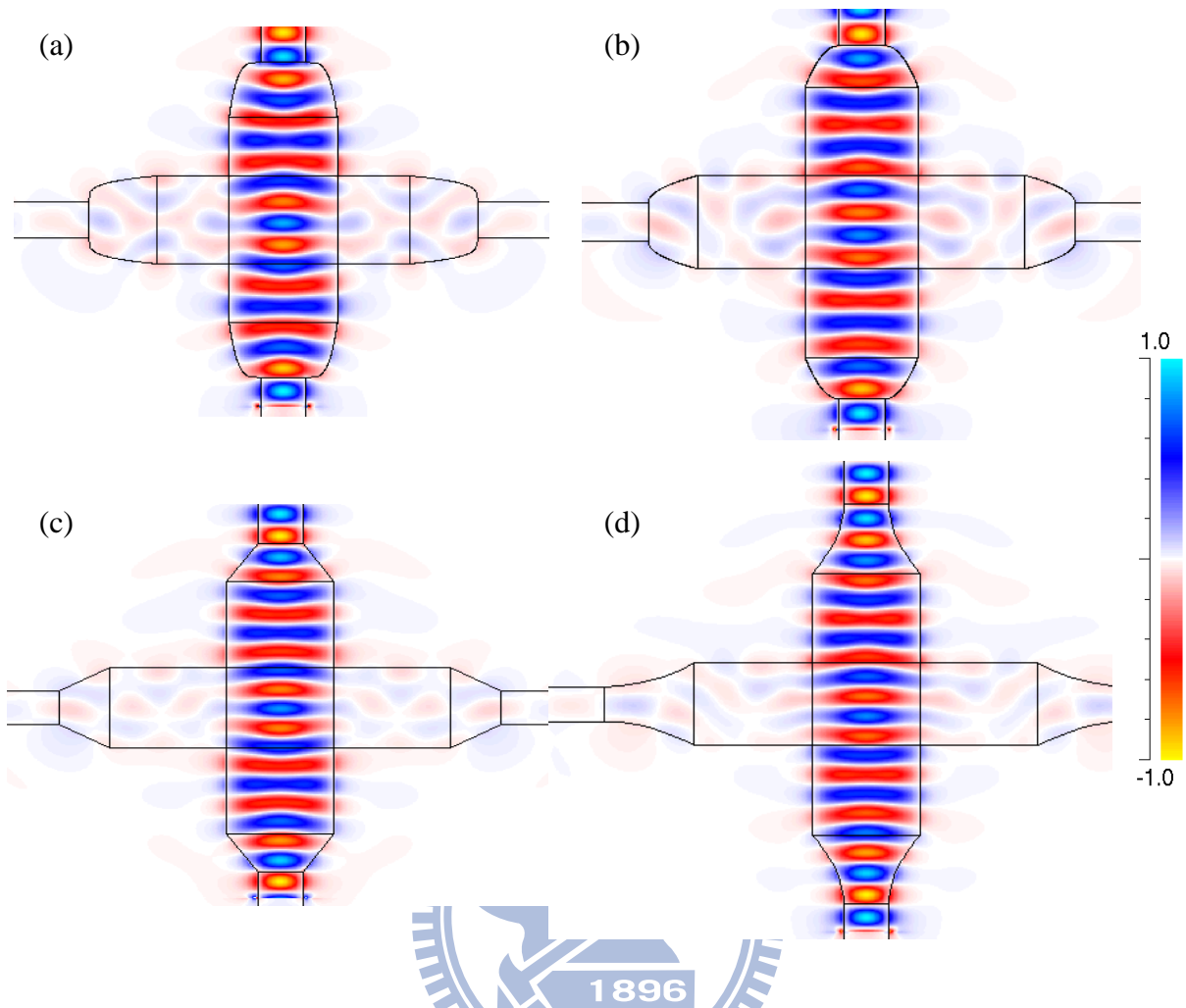Figure 3.6-2 FDTD simulations of the input guided mode propagation through
MMI based waveguide crossings sandwiched by four different tapers with (a)
L_t=750nm and n=0.25, (b) L_t=530 nm and n=0.5, (c) L_t=560 nm and n=1 and
(d) L_t=1000 nm and n=2.

Table 2 Performance of waveguide crossings with different taper profiles at the wavelength of
1550 nm

n	L_t (nm)	L_{eff} (nm)	Total length of the crossing L_m+2L_t (nm)	Transition loss (dB)	Insertion loss (dB)	Crosstalk (dB)
0.25	750	1400.0	4300.0	0.17	0.37	-39.83
0.5	530	1735.0	4530.0	0.12	0.33	-42.85
1	560	1889.3	4898.5	0.08	0.24	-45.39
2	1000	1900.0	5800.0	0.02	0.15	-42.34

Figure 3.6-2 exhibits the simulated fields of the input wave propagating through these taper-integrated MMI based crossings with (a) n=0.25, (b) n=0.5, (c) n=1 and (d) n=2. The transverse fields at the junction of the taper and the input waveguide are different but the self-images formed at L_{eff} of the MMI waveguide in these cases have the same beam waist at due to the fixed value of η.

Table 2 summarizes the parameters and performances of simulated taper-integrated MMI based crossings at the wavelength of 1550 nm for the cases of n = 0.25, 0.5, 1 and 2. The lengths of the MMI crossings in the cases of n = 0.25 and n=0.5 are less than twice of the beat length and their insertion loss are lower than that without inserting a taper. Although the dimension of the MMI crossing increases as n increases, the transition loss of the taper decreases and better performance of the waveguide crossing is obtained. In the case of n = 2, the MMI waveguide crossing has the insertion loss of 0.15 dB and the dimension of 5800×5800 nm^2. In addition, the crosstalk in these designs are imperceptible, roughly -40dB.

3.7 Wavelength dependence on insertion loss and crosstalk

Insertion losses and crosstalks of these designed MMI based waveguide crossings with different taper profiles as a function of wavelength are shown in Figure 3.7 (a) and (b). The insertion loss decreases as n increases because the transition losses of the tapers reduce. In each case, the variations of insertion loss is less than 0.1 dB at the wavelength ranging from 1500 to 1600 nm. All the crosstalks of these MMI based crossings are lower than -30 dB at the wavelength ranging from 1500 to 1600 nm. These results indicate these crossings exhibit broad transmission spectra around the wavelength of 1550 nm. In the case of n = 2, the insertion loss is averagely 0.18 dB and the crosstalk is less than -40 dB.
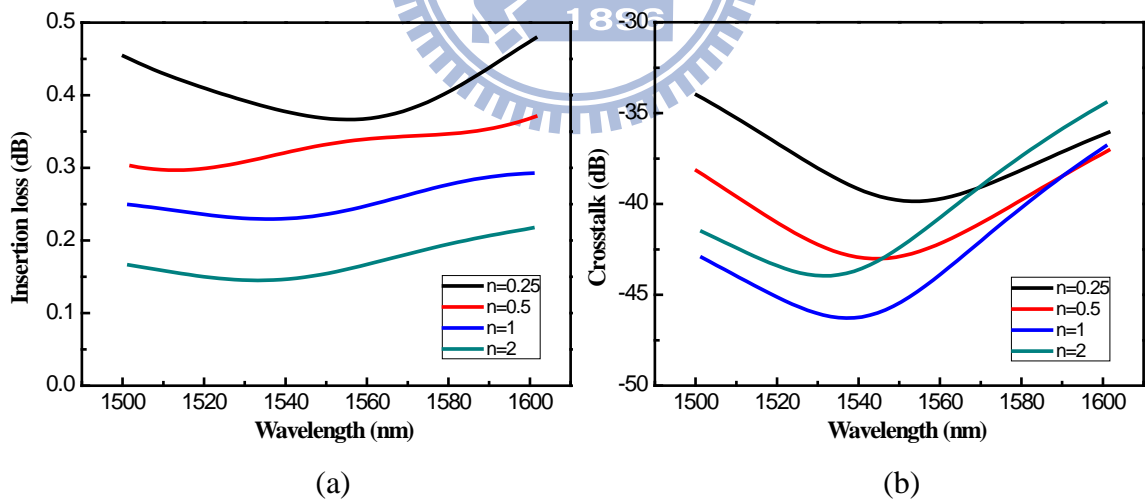

(a)   (b)

Figure 3.7 (a) Simulated insertion loss spectra and (b) calculated crosstalk spectra of the designed MMI-based waveguide crossings for n=0.25 (black curves), 0.5 (red curves), 1 (blue curves) and 2 (green curves)

Chapter 4 Conclusion

In this thesis, we present a novel compact MMI based crossing by using multimode tapers. As a short multimode taper is inserted in between the input/output and MMI waveguides, the transition loss reduces and the length of the required multimode waveguide reduces to be less than twice of the beat length. Besides, the diffraction loss is determined by the profile of the self-image, and its minimum is obtained as η is 0.27.

In the case of using the quadratic taper, the size of the MMI based waveguide crossing is 5800×5800 nm^2, the insertion loss is around 0.15 dB and the crosstalk is lower than -40 dB. In addition, these devices can be fabricated by using standard CMOS fabrication process.
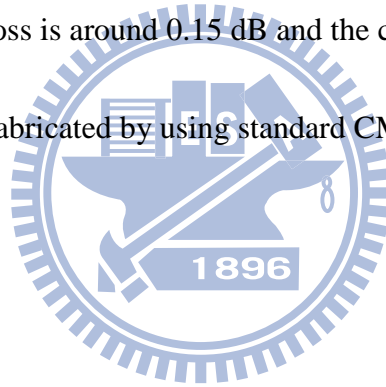
References

[1] P. Koonath, *et al.*, "Monolithic 3-D silicon photonics," *Journal of Lightwave Technology,* vol. 24, pp. 1796-1804, Apr 2006.

[2] B. Jalali, "Can silicon change photonics?," *Physica Status Solidi a-Applications and Materials Science,* vol. 205, pp. 213-224, Feb 2008.

[3] A. S. Liu, *et al.*, "200 Gbps Photonic Integrated Chip on Silicon Platform," in *5th IEEE International Conference on Group IV Photonics*, Sorrento, ITALY, 2008, pp. 368-370.

[4] B. Jalali, *et al.*, "Advances in silicon-on-insulator optoelectronics," *Ieee Journal of Selected Topics in Quantum Electronics,* vol. 4, pp. 938-947, Nov-Dec 1998.

[5] A. G. Rickman, *et al.*, "SILICON-ON-INSULATOR OPTICAL RIB WAVE-GUIDE LOSS AND MODE CHARACTERISTICS," *Journal of Lightwave Technology,* vol. 12, pp. 1771-1776, Oct 1994.

[6] L. Liao, *et al.*, "High speed silicon Mach-Zehnder modulator," *Optics Express,* vol. 13, pp. 3129-3135, Apr 2005.

[7] Y. M. Kang, *et al.*, "Monolithic germanium/silicon avalanche photodiodes with 340 GHz gain-bandwidth product," *Nature Photonics,* vol. 3, pp. 59-63, Jan 2009.

[8] H. S. Rong, *et al.*, "An all-silicon Raman laser," *Nature,* vol. 433, pp. 292-294, Jan 2005.

[9] H. S. Rong, *et al.*, "A continuous-wave Raman silicon laser," *Nature,* vol. 433, pp. 725-728, Feb 2005.

[10] T. Fukazawa, *et al.*, "Low loss intersection of Si photonic wire waveguides," *Japanese Journal of Applied Physics Part 1-Regular Papers Short Notes & Review Papers,* vol. 43, pp. 646-647, Feb 2004.

[11] W. Bogaerts, *et al.*, "Low-loss, low-cross-talk crossings for silicon-on-insulator nanophotonic waveguides," *Optics Letters,* vol. 32, pp. 2801-2803, Oct 2007.

[12] P. Sanchis, *et al.*, "Highly efficient crossing structure for silicon-on-insulator waveguides," *Optics Letters,* vol. 34, pp. 2760-2762, Sep 2009.

[13] W. Q. Ding, *et al.*, "Compact and low crosstalk waveguide crossing using impedance matched metamaterial," *Applied Physics Letters,* vol. 96, Mar 2010.

[14] H. L. Liu, *et al.*, "Low-loss waveguide crossing using a multimode interference structure," *Optics Communications,* vol. 241, pp. 99-104, Nov 2004.

[15] H. Chen and A. W. Poon, "Low-loss multimode-interference-based crossings for silicon wire waveguides," *Ieee Photonics Technology Letters,* vol. 18, pp. 2260-2262, Nov-Dec 2006.

[16] L. B. Soldano and E. C. M. Pennings, "OPTICAL MULTIMODE INTERFERENCE DEVICES BASED ON SELF-IMAGING - PRINCIPLES AND APPLICATIONS," *Journal of Lightwave Technology,* vol. 13, pp. 615-627, Apr 1995.

[17] K. S. Yee and J. S. Chen, "The finite-difference time-domain (FDTD) and the finite-volume time-domain (FVTD) methods in solving Maxwell's equations," *Ieee Transactions on Antennas and Propagation,* vol. 45, pp. 354-363, Mar 1997.